Cell atlas of the developing human meninges reveals a dura origin of meningioma

Elin Vinsland[1,#], Sergio Marco Salas[2,3], Ivana Kapustová[1], Lijuan Hu[1], Simone Webb[4,5], Xiaofei Li[6], Xiaoling He[7], Mats Nilsson[2], Muzlifah Haniffa[5], Roger Barker[7], Oscar Persson[8,9], David R. Raleigh[10], Erik Sundström[6], Peter Lönnerberg[1], Sten Linnarsson[1,11,#]

#Corresponding authors: elin.vinsland@ki.se , sten.linnarsson@ki.se

1. Laboratory of Molecular Neurobiology, Department of Medical Biochemistry and Biophysics, Biomedicum, Karolinska Institutet, 17177 Stockholm, Sweden
2. Science for Life Laboratory, Department of Biochemistry and Biophysics, Stockholm University, Solna, 17154 Stockholm, Sweden
3. Institute of Computational Biology, Computational Health Center, Helmholtz Munich
4. Biosciences Institute, Newcastle University, Newcastle upon Tyne NE2 4HH, UK
5. Wellcome Sanger Institute, Wellcome Genome Campus, Hinxton, Cambridge CB10 1SA, UK
6. Division of Neurodegeneration, Department of Neurobiology, Care Sciences and Society, Karolinska Institutet, Solna, Sweden
7. John van Geest Centre for Brain Repair, Department of Clinical Neurosciences, Cambridge Stem Cell Institute, University of Cambridge, Cambridge, UK
8. Department of Clinical Neuroscience, Karolinska Institute, 17177Stockholm, Sweden
9. Department of Neurosurgery, Karolinska University Hospital, 17164 Stockholm, Sweden
10. Departments of Radiation Oncology, Neurological Surgery, and Pathology, University of California San Francisco, San Francisco, California, USA
11. Lead contact

HIGHLIGHTS

- scRNA-seq and spatial transcriptomics reveals architecture of human fetal meninges development
- Meningeal layers are formed concurrently, by a gradual refinement of cell states
- A *CDH1*+ inner dura sublayer expresses tight junction genes like the arachnoid barrier
- Meningioma tumours likely originate from inner dura lineage cells, not arachnoid

SUMMARY

The vertebrate central nervous system is enveloped by the meninges, consisting of the pia, arachnoid, and dura layers. The arachnoid is hypothesised to give rise to the most common primary intracranial tumours, meningiomas. However, molecular evidence supporting this hypothesis is lacking. There are no effective medical therapies to treat meningiomas that are resistant to local interventions, encumbered by our limited understanding of their cellular origin. To address this limitation in our understanding of meningioma biology, we generated a comprehensive reference single cell and spatial transcriptomic atlas of human fetal meninges at post-conceptional weeks 5-13. We found that the meningeal layers develop concurrently, and identified an inner *CDH1*-positive dura cell layer expressing tight junction genes consistent with barrier function. We show that transcriptionally, meningioma cells resemble dura-lineage cells, and that common meningioma driver genes were expressed preferentially in the dura lineage. Our findings suggest that meningiomas originate from dura lineage cells.

KEYWORDS

Meninges, meningeal layers, meningioma, single-cell, spatial transcriptomics, fibroblasts, arachnoid barrier, dura, FOXC1, choroid plexus

INTRODUCTION

The vertebrate central nervous system (CNS) is enveloped by the meninges, comprising the pia, arachnoid and dura matres. The meninges attach the brain to the skull, supply blood flow and immune protection, and provide space through which cerebrospinal fluid flows around the brain. Several CNS developmental defects result from aberrations of the meninges, for example those caused by *FOXC1* mutations[1]. Importantly, the meninges give rise to the most common primary intra-cranial tumours, meningiomas. Although commonly benign or low grade, there are no effective medical therapies for higher-grade atypical or anaplastic meningiomas that are resistant to standard interventions[2], partly due to our limited understanding of meningioma biology.

Meningioma tumours arise from meningeal cells, but the precise cell type of origin is not fully known. John Cleland (1864) first described meningioma as a tumour of the arachnoid granulations, which are protrusions of the arachnoid mater into the dural venous sinuses that drain cerebrospinal fluid into venous blood. Martin Schmidt (1902) showed that meningioma cells can resemble arachnoid cap cells, which form whorls and psammoma (sand-like) bodies on the perimeter of arachnoid granulations. The influential neurosurgeon Percival Bailey (1931) agreed, noting that meningioma tumours often cause a gritty sound when cut, due to the presence of numerous psammoma bodies. Contemporary authors generally concur with the arachnoid cap cell origin[3]. However, the cell of origin has only been inferred based on anatomical, histological and morphological similarities, while molecular or genetic evidence is lacking. In mouse models, there is evidence that some meningiomas can be generated from *PTGDS*-expressing primordial meningeal cells[4], but it remains unknown if *PTGDS* identifies a progenitor population in human meninges, or if such cells give rise to meningiomas. Furthermore, recent evidence suggests other cell types could contribute to the earliest stages of meningeal tumorigenesis too, such as *NOTCH3*+ mural cells[5].

In other tumours, the cell of origin has been inferred from transcriptional similarity to normal cell types, for example based on single-cell atlases[6]. While efforts to map the cellular architecture of the meninges have increased in recent years, few studies have specifically focused on the meninges and meningeal fibroblasts. The first such effort performed single-cell RNA sequencing (scRNA-seq) of embryonic day (E) 14.5 *Col1a1* positive cells in mice, and shed initial light on fibroblast heterogeneity within the pia, arachnoid, and dura maters[7]. This was followed by a scRNA-seq study of the human adult dura[8], and the adult mouse and human leptomeninges (pia and arachnoid)[9,10]. Other studies incidentally had parts of the meninges in their datasets while sampling the brain[11,12], or focused their analysis on the cranium[13,14], or immune cells[15].

Furthermore, tumours tend to hijack developmental mechanisms[6,16,17], and the region and severity of meningioma tumours correlate with the embryonic origin of the meninges. The meninges are thought to originate from mesoderm and the neural crest. In accordance, meningioma tumours resulting from *NF2* mutations originate mostly from neural crest-derived convexity meninges, where tumours are also more frequently classified as high-grade compared to mesoderm-derived skull-base meningiomas[17]. Therefore, understanding the molecular determinants of meningeal origin and development are key to identify the drivers of growth and transformation of meningiomas. Despite the clinical importance of meningeal origin for meningioma biology, no comprehensive cell atlas has been published covering the developing human meninges. As a result, not much is known about how the human meninges develops either, such as the genesis of meningeal layers by fibroblasts, their maturation over developmental timepoints, and in co-development and differentiation of other cells in the meninges, like immune cells and vasculature.

Here, we therefore set out to survey the development of human meninges, from embryonic post-conceptional week (PCW) 5-8 and fetal PCW 9-13 (hereafter PCW 5-13 collectively referred to as 'fetal'), by scRNA-seq and probe-based *in situ* gene expression analysis (Xenium, hereafter 'spatial transcriptomics'; Fig. 1A). We also collected published bulk RNA-seq and scRNA-seq data for human meningiomas[18], and generated new spatial transcriptomic data for seven such tumours (Fig. 1B).

Below, we carefully and comprehensively describe our cell atlas of the developing meninges, focusing on immune cells, vascular cells, and importantly, fibroblasts. We then use well-annotated fibroblast cell types and gene expression programs that are active during normal meningeal development as a blueprint to understand the cell of origin and cellular composition of human meningiomas (Fig. 1C).

RESULTS

Comprehensive cellular and spatial atlas of the developing human meninges

For scRNA-seq, we collected 16 human meninges samples from 13 donors across PCW 5-13. We collected the whole meninges that peeled off the brain (SFig. 1A-B). A total of 156,726 high-quality cells were used for further analysis (Fig. 1A). The mean UMI per sample was 8,842. As expected, anucleated erythropoietic cells showed the lowest gene and UMI counts (SFig. 1C); excluding those cells, the mean UMI count was 10,249 (Table S1). An analysis of the distribution of maternal and paternal SNP alleles[19] (Methods) indicated that some erythrocytes were maternal, while all other cells were fetal (SFig. 1D). We found that the data was well-integrated across samples even in the absence of batch correction, which we therefore omitted in order to avoid suppressing true biological variation (SFig. 1E-F).

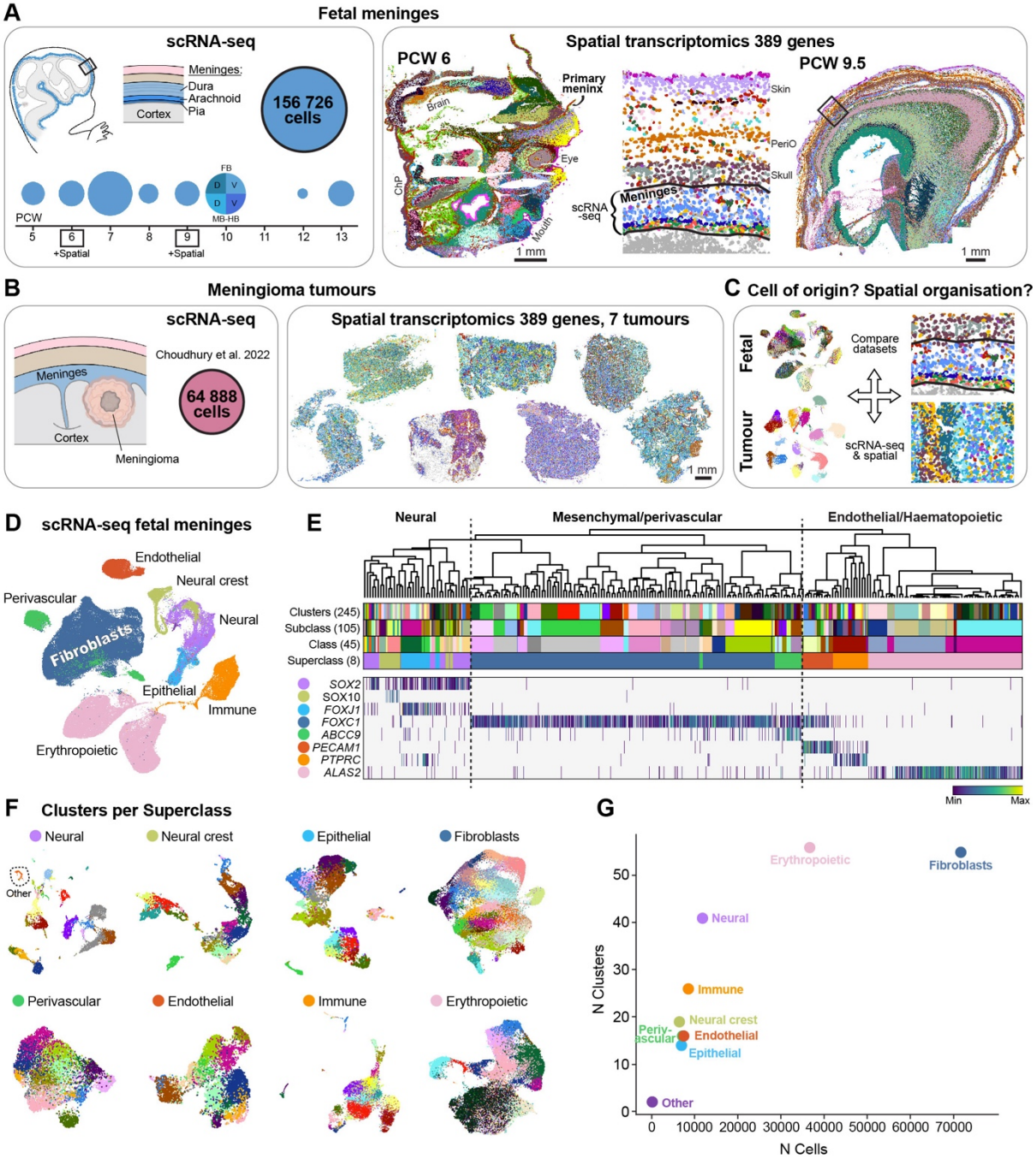

Figure 1. Cellular and spatial atlas of the developing human meninges
(A) Data from fetal meninges. Left: Number of cells collected from PCW 5-13 meninges for scRNA-seq (totally 156,726 cells passing QC). Right: Spatial transcriptomics of sagittal sections of PCW 6 and 9.5 heads. Polygons are segmented nuclei coloured by clusters. Lines define the meninges and where scRNA-seq data was collected.
(B) Data from meningioma tumours. Left: scRNA-seq data downloaded from Choudhury et al. (2022)[18]. Right: Spatial transcriptomics performed in this study on seven tumours.
(C) Strategy to compare scRNA-seq and spatial data from fetal meninges and meningioma tumours, to study conserved developmental cell types in meningioma.
(D) UMAP embedding of scRNA-seq data from fetal meninges coloured by Superclass.
(E) Dendrogram of scRNA-seq data with attributes from top to bottom: 245 clusters, 105 Subclasses, 45 Classes, and 8 Superclasses; coloured as in (D), heatmap showing gene expression marking neural cells (*SOX2*), neural crest (*SOX10*), ependymal cells (*FOXJ1*), meningeal fibroblasts (*FOXC1*), pericytes (*ABCC9*), endothelial cells (*PECAM1*), immune cells (*PTPRC*), and erythropoietic cells (*ALAS2*).
(F) UMAPs of each Superclass coloured by clusters.
(G) Scatter plot of number of cells and number of clusters per Superclass.

We generated a total of 245 clusters (Methods), annotated to four levels of detail: cell type (n=115), subclass (n=105), class (n=45), and superclass (n=8). We computed metadata such as cell cycle score, fetal age, and enriched genes for each cluster (Table S2). Since the meninges are a connective tissue, the biggest superclass consisted of *FOXC1*+ fibroblasts, which made up half the dataset. We also identified *PECAM1*+ endothelial, *ABCC9*+ perivascular, *PTPRC*+ immune, and *ALAS2*+ erythropoietic cells in the meninges. Probably, by peeling the meninges off the brain for sequencing, we also acquired interacting *SOX2*+ neural, *SOX10*+ neural crest and *FOXJ1*+ epithelial (choroid plexus) cells (Fig. 1D-G). Due to the diversity of the dataset presented here, we were able to generate highly specific markers for many cell types of the meninges (SFig. 1G).

We used spatial transcriptomics to validate and locate cell types identified in the scRNA-seq data. To keep the meninges anatomically intact we cryosectioned whole heads at PCW 6 and PCW 9.5. Two medio-lateral sagittal sections from PCW 6 and one lateral sagittal section from PCW 9.5 were analysed, with a custom probe-set targeting 389 genes (Table S3) selected based on the fetal scRNA-seq data. We generated 53 and 50 clusters respectively, after single nucleus segmentation at the two ages (SFig. 1H-I, Table S4). At PCW 6, we found diverse populations of craniofacial mesenchyme, neural crest-derived tissues, progenitors and differentiating neural cells of the CNS (in the forebrain, midbrain, hindbrain, eye), choroid plexus, and vascular and immune cells. Importantly, we identified the earliest described layer of the meninges; the primary meninx (SFig. 1H). At PCW 9.5, clustering highlighted a remarkably complete stack of layers spanning the developing cortical layers from the ventricular zone to Cajal-Retzius cells in the cortical plate, to fibroblasts of the meninges, future skull, periosteum, skin and surface periderm (more in Figure 4). We also noted scattered populations of immune cells (for example active and classical monocytes, macrophages, mast cells, microglia), Schwann cells (melanocytic lineage), and various vascular cells, among others (SFig. 1I).

In the following sections, we analysed each superclass of meningeal cells — immune, vascular (Box 1), and fibroblasts — focusing on their heterogeneity and maturation during meninges development.

Fetal immune heterogeneity and B-lineage cells from PCW 5

The fetal meninges harboured a surprisingly heterogeneous population of immune cells across PCW 5-13, including at the earliest stages. We identified 19 cell types of myeloid and lymphoid origin (Fig. 2A-B, SFig. 2A). Except for three cells, all immune cells were of fetal origin (Fig. 2C). By including canonical markers and enriched genes from our scRNA-seq dataset (Fig. 2E, Table S2) in the spatial transcriptomics panel (Table S3), we validated and located those immune cells in the primary meninx at PCW 6, and leptomeninges and dura at PCW 9.5 (Fig. 2D-G).

Macrophages were the most abundant (Fig. 2H), with plentiful IBA1+ cells concentrated around the primary meninx/leptomeninges at PCW 6 and 9.5 (SFig. 2B). Notably, IBA1 staining of meninges revealed a uniform sparse tiling of macrophages in en face floating sections (SFig. 2C), consistent

with repelling mechanisms controlling their location. The leptomeninges defined an anatomical barrier where microglia (*CX3CR1*, *P2RY12*, *C3*) always resided on the brain side, while monocytes/macrophages (*CD14*, *MRC1*) resided in the leptomeninges and the rest of the head, already from PCW 6 in relation to the primary meninx (Fig. 2F). Microglia were also concentrated inside the developing eye, while monocytes/macrophages resided outside, except one macrophage inside a ring of endothelial cells at the very centre (SFig. 2D).

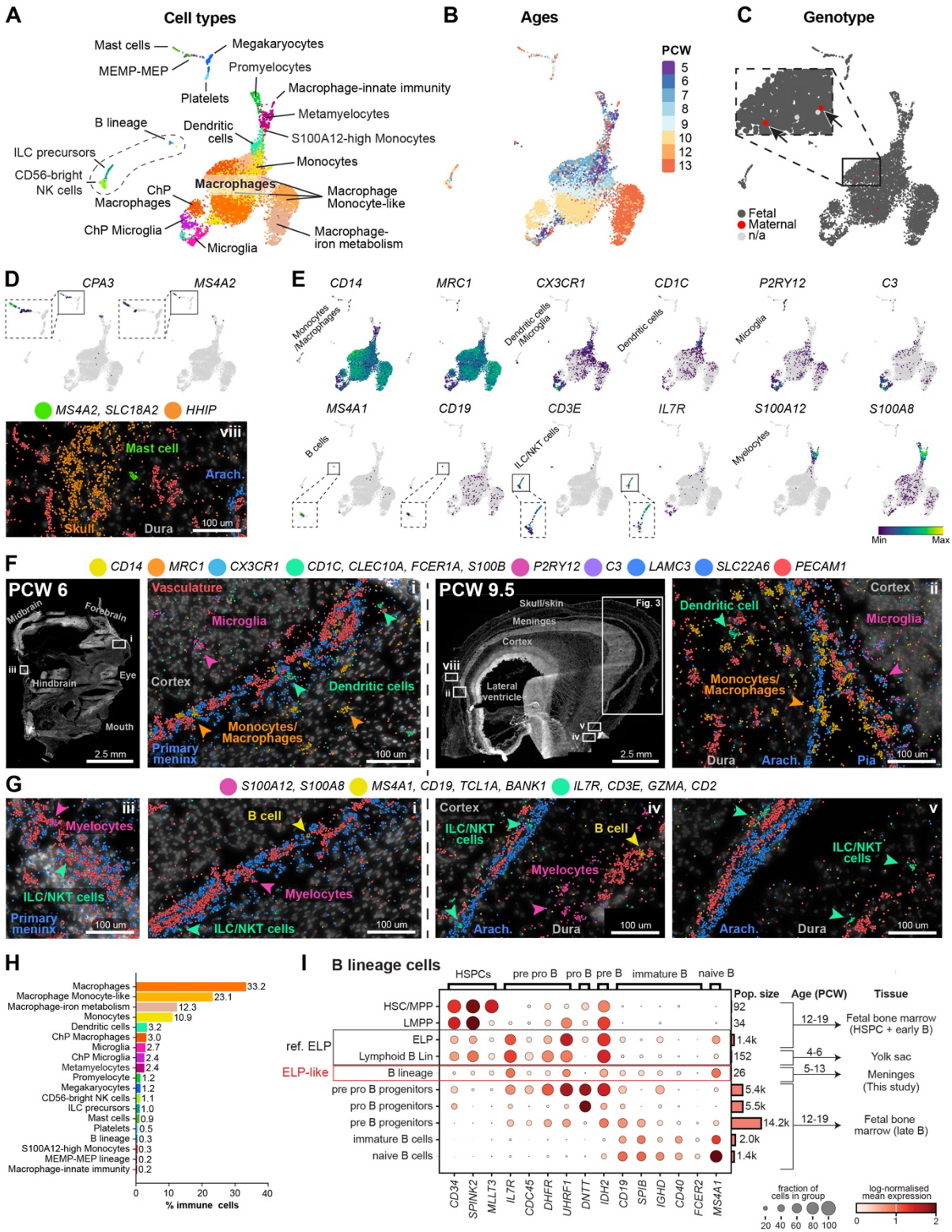

Figure 2. Immune cell diversity in the developing meninges
(A) UMAP coloured by clusters of annotated immune cells. MEMP, megakaryocyte erythroid mast cell progenitor; MEP, megakaryocyte erythroid progenitor.
(B) UMAP coloured by sample age.
(C) UMAP coloured by maternal/fetal genotype, by maternal/paternal SNP analysis (Methods). Inset highlights two maternal immune cells (arrows).
(D) UMAPs coloured by gene expression on a grey background of all cells, and spatial transcriptomics at PCW 9.5, of mast cell markers.
(E) UMAPs coloured by gene expression of immune cell markers.
(F) Spatial transcriptomics of PCW 6 and 9.5 fetal heads, showing RNA molecules on DAPI. Marker genes for microglia, monocytes/macrophages, and dendritic cells are shown, coloured as in (A).
(G) Same as (F) but for ILC/NKT cells, B-cells, and the myelocytic lineage.
(H) Percentage of immune cell types, coloured as in (A)
(I) Dot plot of scRNA-seq gene expression of B-lineage markers across developmental tissues (fetal bone marrow as B-cell reference[22] vs yolk sac[21], and meninges (this data)). The size of the dot represents the % of cells within a group that express a given gene, and the colour of the dot indicates ln(x+1) mean gene expression within the group, where x equal counts normalised to 1e4 per cell.
ELP, early lymphoid cell; HSCs, haematopoietic stem cell.

There is growing evidence for B lymphoid cell presence in early human development. Recent investigations into the fetal B-cell developmental hierarchy defined *CD34+IL7R+CD19-* early lymphoid progenitors (ELP) in human fetal liver as early as PCW 6[20]. Another report detailed the yolk sac 'Lymphoid B lineage' from PCW 4-6[21]. These data raise the intriguing possibility that adaptive lymphoid cells are generated and established in peripheral organs as early as PCW 6. However, the earliest timepoint of establishment of lymphoid cells has not been determined in the embryonic head and meninges. B-lineage cells made up 0.3% of immune cells in the meninges (Fig. 2H) and were clearly distinct from innate lymphoid subtypes (ILC precursors and CD56-bright NK) (SFig. 2E-F). Our scRNA-seq data confirmed that *CD34+IL7R+CD19*-low ELP-like B-lineage cells were transcriptionally similar to second trimester fetal bone marrow ELPs[22], where B cells are well-described to differentiate and diversify (Fig. 2I). We confirmed ELP presence in embryonic meninges as early as PCW 5, and up until about PCW 7, after which point (PCW 8-13) the meningeal B-lineage appeared to differentiate and acquire more mature markers for pre pro-, pro-, pre-, and immature B cells (SFig. 2G).

These data position the meninges as a contributor to the first and second-trimester differentiation and diversification of human B cells, which has recently been appreciated as present in the fetal liver[23], and a key function of the fetal bone marrow[22]. Further, we demonstrate B cell presence in the embryonic meninges one week earlier in gestation than previously reported for liver tissue.

BOX 1 Fetal meningeal vasculature and choroid plexus

Meninges contribute to brain vascularisation, and have early PROX1+ lymphatic-like endothelial cells

The fetal meninges contained perivascular cells such as pericytes, smooth muscle cells, and perivascular fibroblasts (Fig. 3A), as well as vascular endothelial cells (Fig. 3B), across PCW 5-13 (Fig. 3C). The endothelial cells expressed stereotypical genes involved in arterio-venous zonation (Fig. 3D-E), as previously described in both mouse and human[24–27], and also contained *COL15A1+ ESM1+* tip cells (Fig. 3D). Over time, endothelial cells transitioned from the primary vascular plexus at PCW 5, to arterial and venous capillaries around PCW 7-9, and larger arterioles and venous lymphatic-like cells at PCW 12-13. However, the forebrain didn't have venous capillaries even at PCW 13 (Fig. 3E), indicating that this vascular specification occurred earlier in the meninges. Immunostaining of smooth muscle actin (*ACTA2* gene) showed that larger arteries were present in the leptomeninges, dura and skin at PCW 9.5 (Fig. 3F-G).

Most endothelial cells in the meningeal scRNA-seq dataset expressed the transcription factor *FOXQ1* (Fig. 3D), which controls differentiation of blood brain barrier (BBB) endothelial cells in mice[28]. Spatial transcriptomics showed that while *PECAM1* was expressed in all endothelial cells in the head, *FOXQ1* was uniquely expressed in endothelial cells below the arachnoid, and extending into the brain (Fig. 3H). This was observed as early as PCW 6 and together with the primary meninx (Fig. 3I).

The cellular ontogeny of meningeal lymphatic vessels is still unclear[29]. We found that *ACKR1+ LYVE1+* venous cells expressed the key lymphatic transcription factor *PROX1*[30–32] (Fig. 3D). Spatially, *PROX1+ FOXQ1+* endothelial cells were present below the arachnoid, and *PROX1+ FOXQ1-* endothelial cells in the developing skin at PCW 9.5 (Fig. 3H & 3J). These observations suggest that (1) meningeal lymphatic cells were mostly derived from the venous endothelium, and (2) subarachnoid lymphangiogenesis may have started in early fetal development, surprisingly so, since meningeal lymphatics develop postnatally in mice[33].

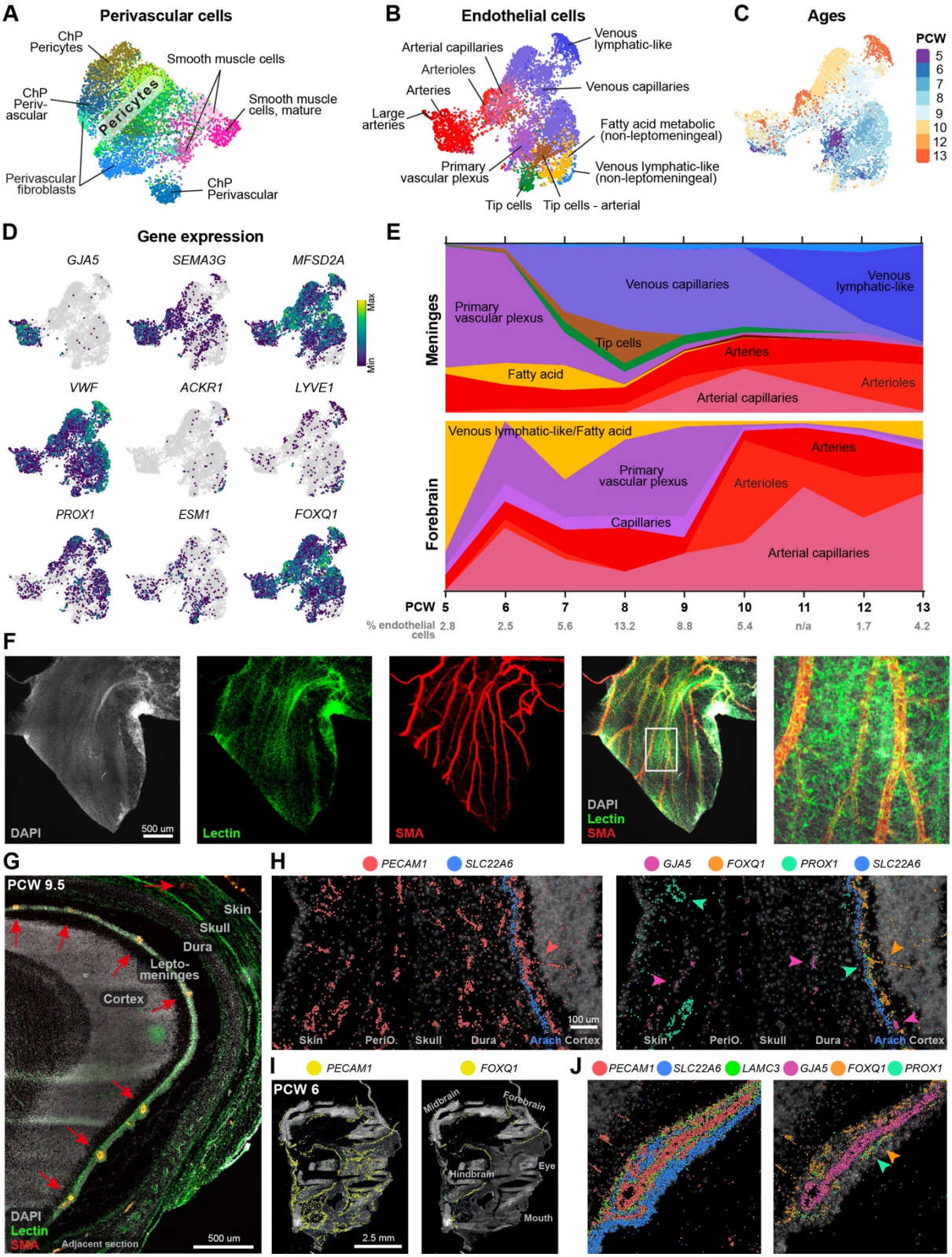

Figure 3. Vasculogenesis in the meninges and brain
(A) UMAP of perivascular cells.
(B) UMAP of endothelial cells, coloured by arterio-venous zonation.
(C) UMAP of endothelial cells coloured by sample ages.
(D) Gene expression of arterio-venous zonation markers, lymphatic- and tip cells.
(E) Proportion of endothelial cell types by age, in the meninges and forebrain12.
(F) Lectin dye (vasculature), DAPI (nuclei), and Smooth muscle actin (SMA) immunostaining in a PCW 9.5 floating meninges.
(G) Same as (F) but in a sagittal section (red arrows point to arteries).
(H) Spatial transcriptomics of all endothelial cells (PECAM1), arteries (GJA5 & pink arrows), venous lymphatic-like cells (PROX1 & mint-green arrows), leptomeninges and brain-specific endothelial cells (FOXQ1 & orange arrows) and arachnoid (SLC22A6) in a PCW 9.5 head. Coloured dots represent RNA molecules.
(I) Spatial transcriptomics of PECAM1 and FOXQ1 in a PCW 6 head.
(J) Same as (H) but with pia (LAMC3), around an artery.

Choroid plexus ciliogenesis and unique PTPRC+ fibroblasts

CSF is generated by filtration of blood at the choroid plexus (ChP), filling the brain ventricles and subarachnoid spaces. Using spatial transcriptomics, we noticed that three layers comprising the *FOXC1+* primary meninx, the underlying endothelial cells, and the *FOXJ1+* ependymal cells were continuous with the corresponding three layers of the emerging ChP at PCW 6 (SFig. 3A). At PCW 9.5, the characteristic inside-out anatomy of the ChP had been formed from those initial three layers, with a ChP epithelium surrounding a stroma of meningeal and vascular cells (SFig. 3B-D). There were also erythropoietic cells, immune cells, and perivascular cells in the ChP. The meningeal fibroblasts in the ChP were mostly pial (SFig. 3C). ChP endothelial cells were mostly *FOXQ1-* (i.e. outside brain and leptomeninges), though there were a few *FOXQ1+* cells (brain-leptomeningeal BBB endothelial cells) too (SFig. 3E). Microglia always resided in the ChP epithelial layer, whilst macrophages were in the stroma, just like the brain versus meninges (SFig. 3F).

The ChP epithelium develops by differentiation from adjacent neuroepithelium (future multiciliated ependymal cells). Our scRNA-seq data comprised 22 clusters of brain and ChP epithelial cells from PCW 5-13 (SFig. 3G-H). While AQP1 immunostaining showed positivity in both brain ependymal cells and the ChP epithelium (SFig. 3D), the serotonin receptor gene *HTR2C* was only expressed in the ChP (SFig. 3I). At the junctions between future ChP epithelium and surrounding neuroepithelium, we identified similar dual neuro-epithelial progenitors and ciliogenesis programs as previously described in mice[34]. These progenitors expressed *RSPO2* and *RSPO3*, followed by *DEUP1* (mouse *Ccdc67*) and *SHISA8* in ciliogenic epithelia, and *AQP1* in fully differentiated ChP epithelia (SFig. 3J-K). We also analysed ChP epithelial cells functionally, by creating a combined CSF gene-set score based on two proteomics datasets from human adult CSF[35,36] (Table S5). CSF genes were indeed expressed in the fetal data, this being greatest in differentiated ChP epithelial cells (SFig. 3L).

We also identified a fibroblast type only present in the ChP, which uniquely expressed *TCF21* (SFig. 3M-N). Both scRNA-seq and spatial transcriptomics showed that they also expressed the immune-related genes *PTPRC* (CD45, pan-leukocyte marker), and *CD38*. However, mouse *Tcf21+Cd38+* fibroblasts did not express *Ptprc* (SFig. 3M).

Our findings demonstrate that human ChP development uses mechanisms that are largely conserved from rodents, but with human-specific features that suggest an evolved role for ChP fibroblasts in immune surveillance at the blood-CSF border.

336 **Fibroblast layer development in the fetal meninges and head**
337
338 Fibroblasts are the principal cells of connective tissues, including the meninges and head
339 mesenchyme. Fibroblasts of the human fetal meninges have previously been described based on
340 basic anatomical, histological and morphological features. However, a comprehensive molecular
341 analysis of head fibroblasts, and the transcriptional cell-type composition of newly forming meningeal
342 layers remain to be elucidated.
343
344 *Fibroblast heterogeneity and organisation in the fetal meninges and head*
345
346 Our scRNA-seq analysis across the PCW 5-13 meninges yielded 71,657 fibroblasts. From this, we
347 generated 55 clusters that we annotated as 29 cell types with distinctly enriched genes (Fig. 4A-B,
348 SFig. 4A, Table S2). 20 of these cell types were classified as fibroblasts of the three meningeal layers;
349 the pia-, arachnoid- and dura mater, their precursors, and the early primary meninx. We also captured
350 other interesting fibroblasts, such as a fibroblast expressing *TAGAP* (a T-cell activating protein),
351 osteogenic fibroblasts (*PTHLH*), chondrocytes (*MATN4*), hindbrain (*HOXA3)* fibroblasts, and the
352 previously mentioned *PTPRC*+ fibroblast unique to the ChP (Fig. 4B-C).
353
354 Next, we charted the distribution of fibroblast cell types *in situ*, in whole heads at PCW 6 & PCW 9.5
355 (Fig. 4D-E). At PCW 6, early craniofacial fibroblasts or mesenchyme were found in well-defined
356 spatial domains like the mesenchyme of extraocular (eyes), maxillary/mandibular (jaws), otic (future
357 ears), and cranial nerve-associated tissues (Fig. 4D). As mentioned before (Fig. 1), we also identified
358 a spatial cluster representing the earliest meninges described in the literature, the primary meninx,
359 from which we had also obtained scRNA-seq data (panels A-C). The primary meninx was a thin layer
360 surrounding the entire brain together with *FOXQ1*+ endothelial cells (Fig. 4D insets i-ii, Fig. 3I), except
361 around the lower ventral hindbrain where a pool of primary meninx, endothelial-, immune-, and
362 erythropoietic cells were found mixed together (Fig. 4D, inset iii). We found that *LAMC3* was uniquely
363 expressed by the primary meninx (SFig. 4B, Table S4). In contrast, the meningeal marker *FOXC1* had
364 a much broader expression in craniofacial fibroblasts at PCW 6, though it became specific to the
365 meninges at PCW 9.5 (SFig. 4B).
366
367 At PCW 9.5, fetal head fibroblasts surrounding the forebrain were already stratified into well-defined
368 layers stacked on top of each other (Fig. 4E, inset iv). Clustering of the spatial data allowed us to
369 identify, from the surface of the head towards the brain, fibroblasts of the skin (periderm, basal
370 epidermis), future skull and periosteum, and the meningeal layers. Other cell types were also present
371 within these fibroblast layers, such as the neural crest-derived Schwann-melanocytic lineage between
372 the periosteum and basal epidermis, lymphatic endothelial cells and pools of erythropoietic cells in the
373 outer periosteum, and classical monocytes mostly in the outer dura. The meninges were divided into
374 eight spatial clusters: five of the outer dura, one inner dura layer, the arachnoid, and the pia.
375
376
377

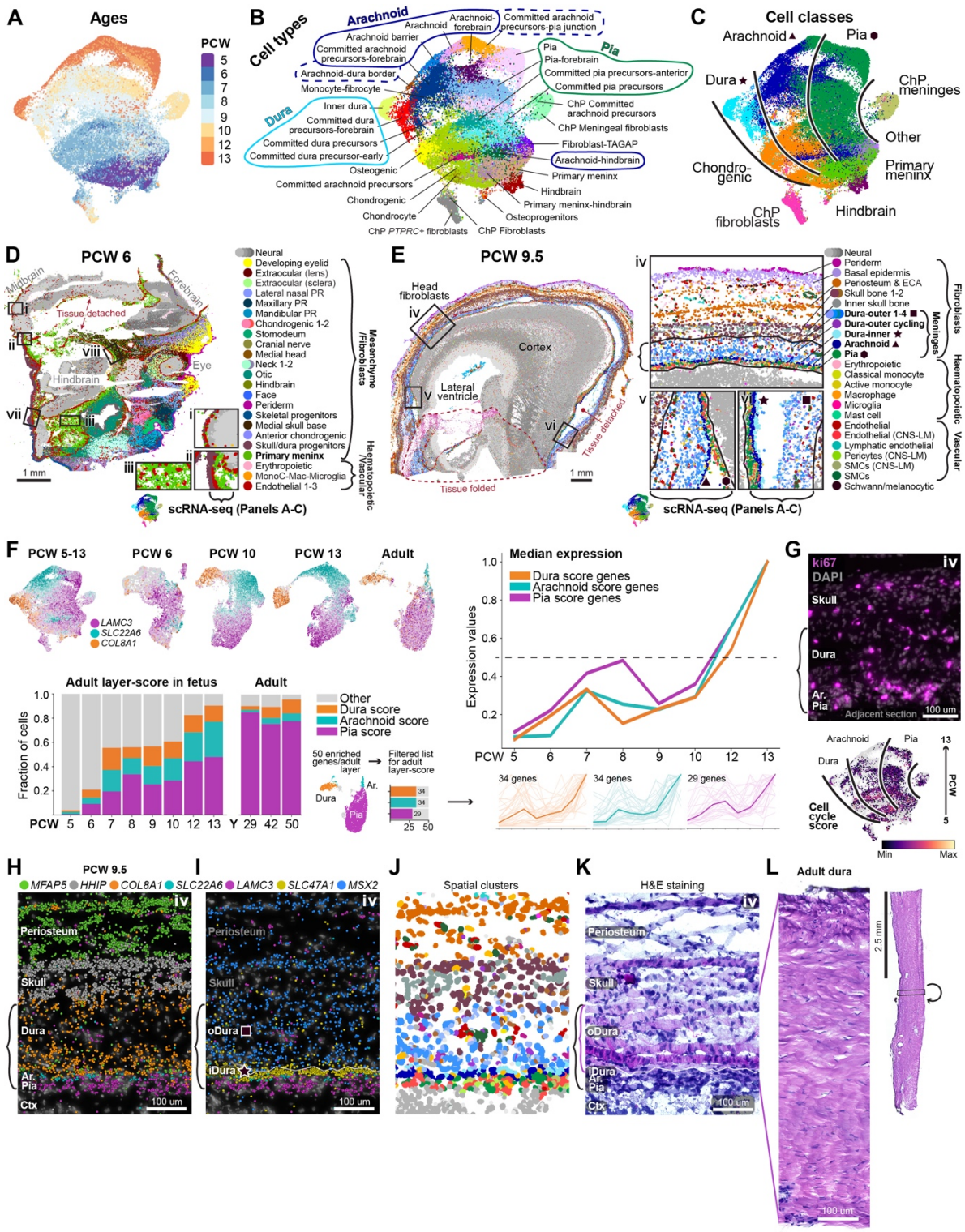
A
Ages
PCW
5
6
7
8
9
10
12
13
B
Cell types
Arachnoid
Arachnoid
Arachnoid-forebrain
Committed arachnoid precursors-pia junction
Arachnoid barrier
Committed arachnoid precursors-forebrain
Arachnoid-dura border
Monocyte-fibrocyte
Pia
Pia-forebrain
Committed pia precursors-anterior
Committed pia precursors
Dura
Inner dura
Committed dura precursors-forebrain
Committed dura precursors
Committed dura precursor-early
ChP Committed arachnoid precursors
ChP Meningeal fibroblasts
Fibroblast-TAGAP
Arachnoid-hindbrain
Osteogenic
Primary meninx
Committed arachnoid precursors
Hindbrain
Chondrogenic
Primary meninx-hindbrain
Chondrocyte
Osteoprogenitors
ChP PTPRC+ fibroblasts
ChP Fibroblasts
C
Cell classes
Arachnoid
Pia
Dura
ChP meninges
Other
Primary meninx
Chondro-genic
ChP fibroblasts
Hindbrain
D
PCW 6
Midbrain
Forebrain
Tissue detached
Hindbrain
Eye
1 mm
Neural
Developing eyelid
Extraocular (lens)
Extraocular (sclera)
Lateral nasal PR
Maxillary PR
Mandibular PR
Chondrogenic 1-2
Stomodeum
Cranial nerve
Medial head
Neck 1-2
Otic
Hindbrain
Face
Periderm
Skeletal progenitors
Medial skull base
Anterior chondrogenic
Skull/dura progenitors
Primary meninx
Erythropoietic
MonoC-Mac-Microglia
Endothelial 1-3
Mesenchyme /Fibroblasts
Haematopoietic /Vascular
scRNA-seq (Panels A-C)
E
PCW 9.5
Head fibroblasts
Cortex
Lateral ventricle
Tissue detached
Tissue folded
1 mm
Neural
Periderm
Basal epidermis
Periosteum & ECA
Skull bone 1-2
Inner skull bone
Dura-outer 1-4
Dura-outer cycling
Dura-inner
Arachnoid
Pia
Erythropoietic
Classical monocyte
Active monocyte
Macrophage
Microglia
Mast cell
Endothelial
Endothelial (CNS-LM)
Lymphatic endothelial
Pericytes (CNS-LM)
SMCs (CNS-LM)
SMCs
Schwann/melanocytic
Fibroblasts
Meninges
Haematopoietic
Vascular
scRNA-seq (Panels A-C)
F
PCW 5-13
PCW 6
PCW 10
PCW 13
Adult
LAMC3
SLC22A6
COL8A1
Adult layer-score in fetus
Adult
Fraction of cells
Other
Dura score
Arachnoid score
Pia score
50 enriched genes/adult layer
Filtered list for adult layer-score
Median expression
Dura score genes
Arachnoid score genes
Pia score genes
Expression values
34 genes
34 genes
29 genes
G
ki67
DAPI
Skull
Dura
Ar.
Pia
Adjacent section
100 um
Arachnoid
Pia
Dura
Cell cycle score
PCW
Min
Max
H
PCW 9.5
MFAP5
HHIP
COL8A1
Periosteum
Skull
Dura
Ar.
Pia
Ctx
100 um
I
SLC22A6
LAMC3
SLC47A1
MSX2
Periosteum
Skull
oDura
iDura
100 um
J
Spatial clusters
K
H&E staining
Periosteum
Skull
oDura
iDura
Ar.
Pia
Ctx
100 um
L
Adult dura
2.5 mm
100 um

Figure 4. Fibroblast layer development in human fetal heads
(A) UMAP of fetal meningeal fibroblasts coloured by sample age.
(B) UMAP coloured by annotated cell types.
(C) UMAP coloured by Class. Black lines separate putative pia, arachnoid, and dura lineages.
(D) Sagittal section of a PCW 6 head coloured by spatial clusters. Three insets show the primary meninx, and where scRNA-seq was sampled. The colour for the primary meninx matches the scRNA-seq Class 'Primary meninx' in (C). Mac, macrophage; MonoC, monocyte; PR, prominence.
(E) Same as (D) but at PCW 9.5. Insets show the meningeal clusters, and where scRNA-seq was sampled. Colours for meningeal layers match those in (C). CNS, central nervous system; ECA, epicranial aponeurosis; LM, leptomeninges; SMC, smooth muscle cells.
(F) Analysis of meningeal layer maturation. Top left: UMAP of all fibroblasts, subsets of PCW 6-, 10-, and 13- (this study), and adult[11] fibroblasts. Cells are coloured by their expression of the gene they express most highly among *LAMC3* (pia), *SLC22A6* (arachnoid), *COL8A1* (dura). Bottom left panel: stacked bar chart showing the fraction of fetal and adult fibroblasts expressing a list of enriched genes from adult pia, arachnoid, and dura (Methods). Y, years. Right panel: median expression of the enriched gene lists over developmental timepoints.
(G) Top: Immunohistochemistry of ki67 and DAPI at PCW 9.5. Inset region 'iv' as in (E), but on an adjacent section. Bottom: scRNA-seq UMAP of fibroblasts coloured by cell cycle score.
(H) Spatial transcriptomics showing layer-specific markers. Brackets indicate the meninges.
(I) Same as (H) but *SLC47A1* (inner dura) and *MSX2* (outer dura, skull and periosteum).
(J) Same region as (H-I) but showing spatial clusters.
(K) H&E staining. Black brackets show the meninges, pink brackets the dura.
(L) H&E staining of adult human dura.

The meningeal layers develop concurrently

Next, we focused on meningeal layer formation over time (Fig. 4F-H). Using the scRNA-seq and spatial transcriptomic data we identified and validated unique markers that can distinguish the pia (*LAMC3*), arachnoid (*SLC22A6*) and dura (*COL8A1*), from PCW 5-13 and in adults (Fig. 4F & H, SFig. 4A). *LAMC3*, which was expressed in the primary meninx at PCW 6, was specifically expressed in the pia in later ages. This indicates that the first meningeal fibroblasts to surround the brain are pia precursors, and/or that the pia develops from the primary meninx. Arachnoid and dura precursors were also present at PCW 5-6, though the emerging spatial organisation of meningeal layers was only found around parts of the hindbrain, in these sections (SFig. 4C). At PCW 9.5, precursors of all three layers covered the entire cortex, and *SLC22A2* which was expressed in more mature arachnoid populations appeared first in the anterior cortex (SFig. 4D).

We wondered if the meningeal layers develop as separate lineages, and if therefore intermediate lineage-specific precursor cell types could be identified, as in haematopoiesis. However, examining the expression of the layer-specific markers *LAMC3*, *SLC22A6* and *COL8A1* in subsets of cells from PCW 6, 10 and 13, instead revealed gene expression gradients and a continuum of pia, arachnoid and dura cells at each age (Fig. 4F top left). The same was true when pooling samples at PCW 5-6, 9-10 and 12-13, ruling out batch effects (SFig. 4E). These observations indicate that the meninges mature as a continuum of cell states, only segregating into distinct layer-specific types at developmental timepoints beyond PCW 13.

To further support this parallel model of meninges development, we created a maturation score based on 50 enriched genes from each adult meningeal layer (Methods) (Fig. 4F bottom left), and examined the temporal emergence of each layer as measured by this score. The analysis revealed that (1) genes expressed by the adult meninges were already expressed in the first trimester, (2) the expression of these genes increased over PCW 5-13, demonstrating a gradual maturation of the meningeal layers, and (3) the pia, arachnoid and dura mature concurrently, not sequentially (Fig. 4F bottom left, and right panel, SFig. 4F). The latter conclusion was also supported by the observation of cycling populations in each layer, by scRNA-seq and Ki67 immunostaining (Fig. 4G). Taken together, these results contradict a branched lineage model as seen in neurogenesis or haematopoiesis. Instead, they support a model where the meningeal layers are formed concurrently, by a gradual refinement of cell states that only segregate into truly distinct layer identities at later developmental timepoints. This latter model resembles how patterning by morphogenetic gradients and cell-cell interactions influence cell fate and layer stratification[37,38].

Identification of an inner and outer dura layer

Next, we investigated the dura in more detail (Fig. 4H-L). Our spatial transcriptomic data identified separate outer and inner layers of the dura (Fig. 4E). While both the outer and inner dura expressed *COL8A1*, the known chondrogenic marker *COL2A1*[13], and dura marker *FXYD5*[7], the inner layer was distinguished by high *SLC47A1* expression (previously attributed to the dura border in mice[9]). The outer dura was distinguished from the inner dura by expression of *MSX2*, which was also expressed in osteogenic tissues like the developing skull and periosteum (Fig. 4H-J, SFig. 4G). We identified a spatial cluster representing the potential common progenitor of these cells which joined the outside of the primary meninx to surround the brain, and expressed *MSX2, HHIP,* and *COL2A1* (Fig. 4D 'Skull/dura progenitors', SFig.4C, Table S4). This suggests that from PCW 5-6, this lineage, together with the primary meninx, give rise to all the meningeal layers. DAPI fluorescence showed a thick outer dura with sparsely located nuclei. However, H&E staining revealed 8-12 sheets of fibroblasts in the outer dura, each a single cell thick, depositing extracellular matrix (ECM) that becomes compact in the adult dura (Fig. 4K-L). These sheets of ECM-embedded fibroblasts extended all the way to the outermost layer of the head, the periderm, and could represent a general mechanism for fibroblast layer formation.

The inner dura expresses many tight-junction genes necessary to form a barrier

The inner layer of the dura comprised a sheet of single cells, apposed onto the arachnoid. In the fetal head, the epithelial marker *CDH1* was expressed in three fibroblast layers: the meningeal barrier separating arachnoid and dura, the outermost periosteal layer (or epicranial aponeurosis) and the periderm (SFig. 5A), raising interesting questions about fibroblast organisation and barrier formation during layer development. Focusing on the meningeal barrier, in mice, *Cdh1* is reportedly only expressed by arachnoid barrier cells[39]. However, in our data, *CDH1* was expressed by both the *SLC47A1*+ inner dura and *SLC22A6*+ arachnoid barrier cells, forming two very closely aligned layers of cells (Fig. 5A-B). The inner dura and arachnoid barrier cells and their precursors also shared expression of other genes, such as *CCN3* (also known as *NOV*), *SLC4A4* and *PTGDS* (Fig. 5A-B). *PTGDS* has been reported to target the arachnoid[40], but *Ptgds-Cre* lineage tracing in mice has shown that it is expressed in the whole meninges[5]. In our data, *PTGDS* expression progressively increased with age in all three layers, including the pia, and inside the more developed parts of the future skull (SFig. 5B-C).

These observations suggest that the inner dura layer may form a functionally distinct epithelial layer attached directly on top of the arachnoid, rather than being a simple continuation of the dura proper. Supporting this idea, the inner dura histologically closely resembled the arachnoid barrier rather than the outer dura (Fig. 5A, H&E). Although not previously reported, we noted further that arachnoid and dura cells in both human adult[11] and mouse fetal meninges[41] also expressed *CDH1* (Fig. 5C), demonstrating that this inner dura layer is an evolutionarily conserved feature that persists into the adult (Fig. 5C). Spatial transcriptomics of human adult dura demonstrated that there existed *CDH1*+ *SLC47A1*+ cells, and that were negative for *SLC22A6* and *SLC22A2* (SFig. 5D).

To form a seal separating the dural and subarachnoid spaces, arachnoid barrier cells express tight- and adherens junctions. Interestingly, we found that genes encoding many of the components of a functional tight junction complex (Fig. 5D-F) were expressed in both the human fetal and adult inner dura (Fig. 5E, olive colour). Key genes included the transmembrane components *OCLN* (Occludin), a few *CLDN*s (Claudins), and *JAM*s, and the intracellular domains *MAGI*s, *TJP*s (Zona Occludens proteins), *PARD3*/*PARD6A-B* (PAR3/PAR6) and *CDC42*. Likewise, genes encoding the core components of adherens junctions were expressed, like *CDH1* (E-Cadherin), *NECTIN*s, *CTNNA/Bs* (α/β-catenin), and *AFDN* (Afadin) (Fig. 5E-F, SFig. 5E-F). Finally, four components of tricellular junctions were also expressed in the inner dura, *MARVELD2* (Tricellulin), *MARVELD3*, *LSR* (Angulin-1), and *ILDR2* (Angulin-3) which together are sufficient to form functional tricellular junction units (Fig. 5E).

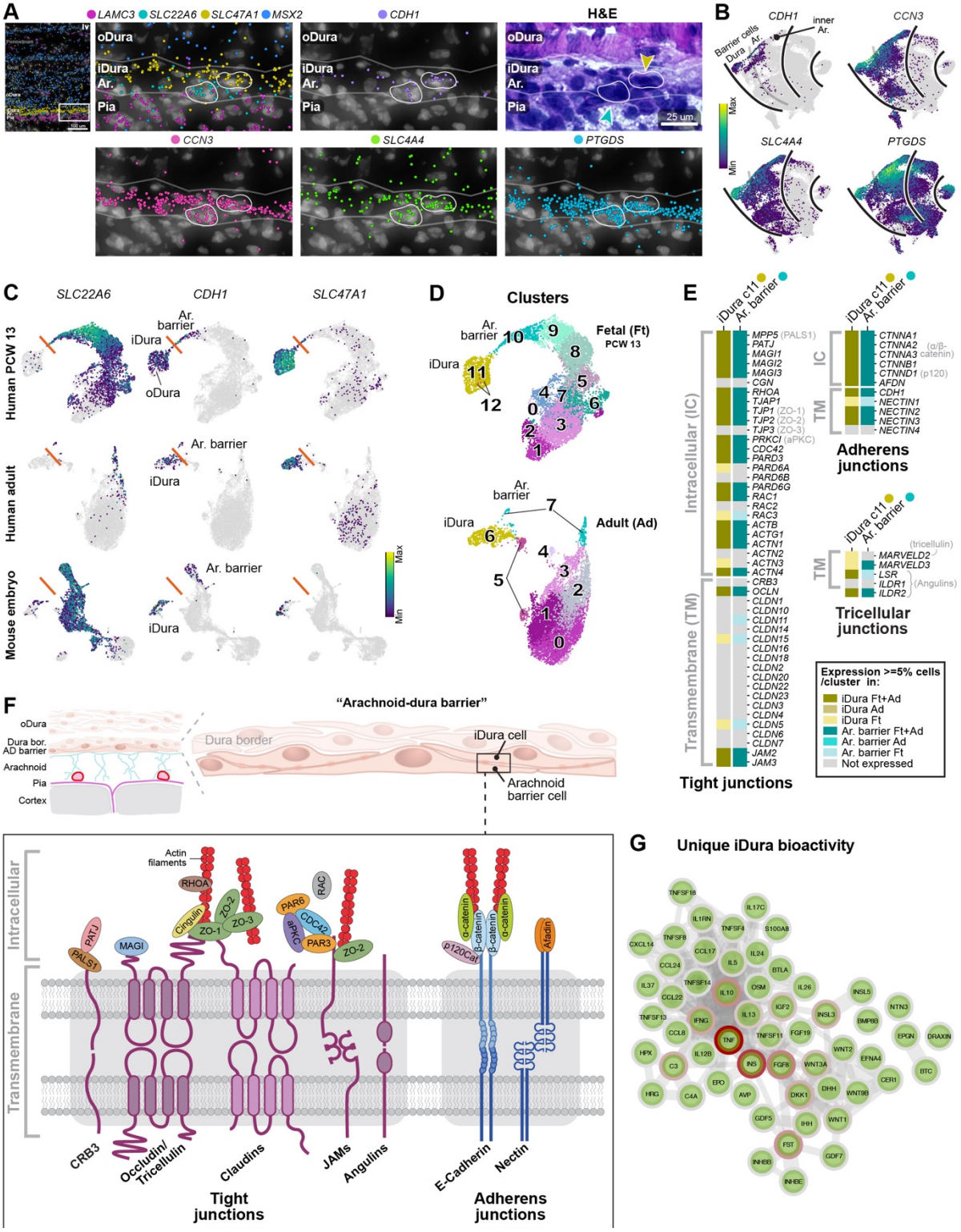
A
LAMC3 SLC22A6 SLC47A1 MSX2
CDH1
H&E
oDura
iDura
Ar.
Pia
25 um
CCN3
SLC4A4
PTGDS
B
CDH1
inner Ar.
Barrier cells
Dura
Ar.
CCN3
SLC4A4
PTGDS
Max
Min
C
SLC22A6
CDH1
SLC47A1
Human PCW 13
Human adult
Mouse embryo
Ar. barrier
iDura
oDura
Max
Min
D
Clusters
Fetal (Ft)
PCW 13
Adult (Ad)
E
iDura c11
Ar. barrier
Intracellular (IC)
Transmembrane (TM)
MPP5 (PALS1)
PATJ
MAGI1
MAGI2
MAGI3
CGN
RHOA
TJAP1
TJP1 (ZO-1)
TJP2 (ZO-2)
TJP3 (ZO-3)
PRKCI (aPKC)
CDC42
PARD3
PARD6A
PARD6B
PARD6G
RAC1
RAC2
RAC3
ACTB
ACTG1
ACTN1
ACTN2
ACTN3
ACTN4
CRB3
OCLN
CLDN1
CLDN10
CLDN11
CLDN14
CLDN15
CLDN16
CLDN18
CLDN2
CLDN20
CLDN22
CLDN23
CLDN3
CLDN4
CLDN5
CLDN6
CLDN7
JAM2
JAM3
Tight junctions
IC
TM
CTNNA1
CTNNA2 (α/β-catenin)
CTNNA3
CTNNB1
CTNND1 (p120)
AFDN
CDH1
NECTIN1
NECTIN2
NECTIN3
NECTIN4
Adherens junctions
(tricellulin)
MARVELD2
MARVELD3
LSR
ILDR1
ILDR2
(Angulins)
Tricellular junctions
Expression >=5% cells /cluster in:
iDura Ft+Ad
iDura Ad
iDura Ft
Ar. barrier Ft+Ad
Ar. barrier Ad
Ar. barrier Ft
Not expressed
F
"Arachnoid-dura barrier"
oDura
Dura bor. AD barrier
Arachnoid
Pia
Cortex
Dura border
iDura cell
Arachnoid barrier cell
Intracellular
Transmembrane
Actin filaments
RHOA
Cingulin
ZO-1
ZO-2
ZO-3
PATJ
PALS1
MAGI
PAR6
CDC42
aPKC
PAR3
RAC
α-catenin
β-catenin
p120Cat
Afadin
CRB3
Occludin/ Tricellulin
Claudins
JAMs
Angulins
E-Cadherin
Nectin
Tight junctions
Adherens junctions
G
Unique iDura bioactivity

Figure 5. Analysis of the arachnoid barrier and inner dura
(A) Spatial transcriptomics of *CDH1*, *CCN3* (also known as *NOV*), *SLC4A4*, and *PTGDS*, and H&E staining. Ar., arachnoid; iDura, inner dura; oDura, outer dura.
(B) Same genes as (A) but coloured on scRNA-seq UMAPs of fibroblasts, on a grey background of all cells. Black lines separate putative pia, arachnoid, and dura lineages.
(C) UMAPs with *SLC22A6* (arachnoid), *CDH1* (barrier cells), and *SLC47A1* (inner dura) expression in human fetal (this study), human adult[11], and mouse embryonic[41] fibroblasts. Orange lines indicate the separation between arachnoid and dura, based on *SLC22A6* expression.
(D) Clusters in fetal PCW 13 fibroblasts (this study) and adult fibroblasts[11]. Cluster colours match the expression of layer-specific genes in (A).
(E) Stylised heatmaps showing the expression of genes encoding core components of tight-, adherens- and tricellular junction complexes, in clusters of fetal and adult inner dura-, and arachnoid barrier cells. Grey text indicates protein names where the gene names are dissimilar.
(F) Schematic illustration of our hypothesis that the arachnoid barrier is created between a layer of arachnoid barrier cells and the inner dura. Tight- and adherens junction proteins produced by genes in (E) are shown, where the proteins left to right are in the same order as in (E) top to bottom, for intracellular and transmembrane domains.
(G) STRING interaction network of a uniquely bioactive gene signature in inner dura. Gene centrality outlined by red.

Based on these observations we propose the possibility that the complete meningeal barrier is formed by two *CDH1*+ layers of cells; the inner dura and the arachnoid barrier (Discussion).

We also found signatures of high bioactivity in the developing meningeal barrier (Table S6). STRING network and pathway analysis showed that the inner dura and arachnoid barrier shared the expression of genes involving a strong IL6-central inflammatory/fibrotic network, PI3K/AKT-, WNT-, and VEGFA/VEGFR2-signaling, developmental biology and axon guidance signatures, EGF-IL6-WNT5A-central cancer pathways, and an IL1B-FN1-central immune network (SFig. 5G). However, inner dura cells uniquely expressed a network of bioactive genes with a strong cytokine and growth factor signature. TNF and INS were the most central genes, followed by FGF8, IL10, FST, C3, and IFNG (Fig. 5G).

Looking at enriched genes in the inner dura and arachnoid barrier, ontologies of shared enriched genes included 'Cell junction' and 'Anchoring junction' (Table S6). Ontologies of uniquely enriched genes in the inner dura represented 'Extracellular matrix' and 'Secreted', while the arachnoid barrier had an enrichment of 'Transport of small molecules' and 'Active transmembrane transporter activity' via solute carriers (SFig. 5H). Therefore, the function of the meningeal barrier may also be questioned if the cellular composition includes inner dura cells.

Meningioma tumours are dura-like

Meningioma tumours are thought to arise from the meningothelial cells of the arachnoid, encompassing both arachnoid cap and barrier cells, based on their histological similarities[3]. However, the discovery of inner dura cells calls into question the precise cell of origin of meningiomas: is it arachnoid meningothelial cells or the inner dura? Like most meningiomas, both cell types expressed *CDH1*. Both also expressed *PTGDS*, and thus cannot be distinguished based on findings in mice, where meningioma can be generated by expression of *NF2* in *PTGDS*-expressing primordial meningeal cells[40]. To address the question, we therefore reanalysed previously published scRNA-seq data[18], and generated new spatial transcriptomic data from seven meningiomas. We compared tumour data to our fetal scRNA-seq and spatial data, and to previously published adult meninges snRNA-seq[11] and bulk[18] datasets.

We processed ten sections from seven meningiomas (six hypermitotic grade 3, one grade 1, Table S1) with spatial transcriptomics using the same gene panel as the fetal samples (Table S3). To allow comparison with fetal meninges, we applied latent Dirichlet allocation (LDA) topic modeling[42] to our scRNA-seq data from PCW 5-13 fibroblasts and perivascular cells (Fig. 6A, SFig. 6A-B). Like clustering, LDA identifies topics — gene modules — that correspond to cell identities. In addition, it

can reveal modules that are shared across cell types, such as cell cycle genes or genes involved in transcriptional reactive states. We generated 35 topics and identified those corresponding to the pia, arachnoid, *PTGDS*+ precursors, inner dura and dura (inner + outer) (Fig. 6A). We also identified one topic shared between arachnoid and inner dura cells; topic #20, 'barrier', with the junctional gene *CDH1* appearing as one of the topic-defining genes (SFig. 6C, Table S7). To validate these inferred topic identities, we transferred the topics to fetal spatial transcriptomic data. In agreement, we found that they were highly active in the corresponding anatomical layers of the meninges. As expected, the barrier topic #20 was shared; i.e. active in both arachnoid and inner dura layers (Fig. 6B-C).

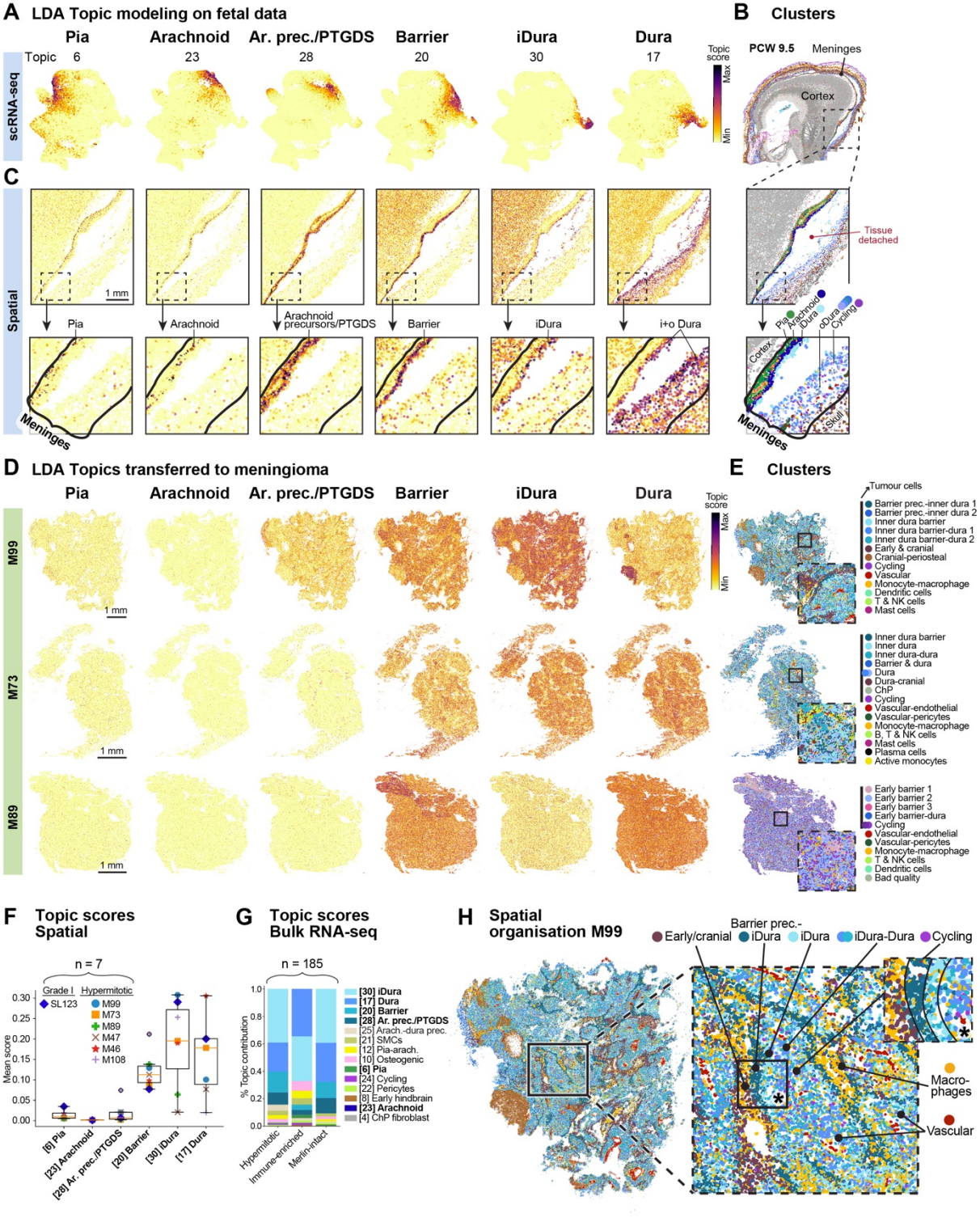

Figure 6. LDA topic modeling in fetal meninges and meningioma tumours
(A) UMAP of fetal fibroblasts and perivascular cells, coloured by their LDA topic score, with topics annotated. Ar. prec., arachnoid precursor; iDura, inner dura; oDura, outer dura.
(B) PCW 9.5 spatial clusters. Insets highlight clusters of meningeal layers.
(C) LDA topics transferred to fetal spatial data. Insets are the same as in (B).
(D) LDA topics transferred to spatial data of grade 3 hypermitotic meningiomas M99, M73 & M89.
(E) Spatial clusters of tumours. Clusters were coloured by their most similar meningeal layer (e.g. inner dura-like cells were coloured cyan, as in (B)).
(F) Boxplots showing scores from LDA topic transfer to spatial data from seven meningiomas.
(G) Stacked bar chart showing scores of LDA topics transferred to bulk RNA-sequencing data from 185 meningiomas, separated into three methylation profiles.
(H) Insets of M99 spatial clusters.

Having thus confirmed that topic modelling identified gene programs specific to meningeal layers, we next transferred the topics to tumour spatial data (Fig. 6D-F, SFig. 6D). Although tumour cells are highly abnormal, we reasoned that the expression of normal gene programs might still reveal their underlying cell identity. As expected, we found that the pia topic was nearly absent. More surprisingly, the arachnoid topic was also absent; in fact, it was the least active topic in every tumour examined. Instead, the most highly activated topics were the inner dura, dura and barrier. Notably, in normal meninges, the barrier topic was shared between arachnoid and inner dura cells, but the absence of arachnoid topic activity in meningiomas argues strongly that tumour cells were not arachnoid. Instead, barrier topic activity in tumour cells coincided with inner dura or dura topics only. Considering the presence of gene programs related to some meningeal layers, this also informed the annotation of meningiomas (Fig. 6E, SFig. 6E). Furthermore, looking at the expression of standard layer markers we did not notice any *SLC22A6* expression (arachnoid), while *CDH1* (barrier) and *SLC47A1* (inner dura) were clearly expressed. Consistently, where *PTGDS* was expressed, it was in non-arachnoid cells (SFig. 6F).

Extending the analysis to a larger cohort of tumours, we transferred our topics to a previously published bulk RNA-seq dataset of 185 meningiomas (hypermitotic, immune-enriched and Merlin-intact subtypes; Fig. 6G, SFig. 6G)[18]. In agreement with the findings from our spatial data, these bulk datasets showed very low activity of pia and arachnoid topics. Instead, inner dura and dura topics dominated, followed by the barrier topic in hypermitotic and merlin-intact meningiomas, and an osteogenic topic in immune-enriched meningiomas. Overall, these observations strongly suggest that meningiomas takes on a predominantly dura cell identity, and indicate a dural-lineage cell as the origin of these tumours.

Furthermore, spatial clustering showed that some, but not all, tumours were highly spatially structured in a manner that resembled a jumbled version of dural and early cranial development (Fig 6H). Tumour cells resembling developmental dural, inner dural and cranial cell types formed nested layers, with vascular and immune cells interspersed. In other tumours, however, cells were mixed more uniformly (Fig. 6E, SFig. 6E). Notably, there were some tumour clusters containing expression of periosteal-, chondrogenic-, and cranial markers (*MFAP5*, *COL2A1*, *HHIP*) (SFig. 6H dotplot, Table S4). These cells had a bone-like appearance with H&E staining (SFig. 6H). Cycling cells, vasculature and macrophages were confirmed with immunohistochemistry, and we also observed that tumours contained lectin-positive non-vascular regions (SFig. 6H). Finally, we collected four human adult dura samples for spatial transcriptomics. The dura samples were obtained from patients with either low-grade glioma or subependymoma, i.e. non-invasive tumours where the meninges should be unaffected ('normal'). While cycling tumour cells expressed *CDH1*, *CCN3*, and *SLC47A1*, and were therefore inner dura-like, the only cycling cells in normal adult dura were vascular, and not dural fibroblasts (SFig. 6H).

The dura lineage specifically expresses genes frequently mutated in meningioma

Further extending our analysis to a previously analysed scRNA-seq dataset of six meningiomas[18] (Fig. 7A), we found that again pia and arachnoid topics were nearly absent and instead barrier, inner dura and dura topics dominated in separate clusters (SFig. 7A-D). We were also able to provide additional annotation to this dataset. For example, our 'Dura-like meningioma' overlapped the previously annotated 'ECM remodelling meningioma', and a subset of pericytes were 'pia-like' (Fig. 7B, SFig. 7A-D). Furthermore, applying an improved karyotyper algorithm (Methods) to this scRNA-seq dataset we found that most cycling cells were derived from tumour MSC6, which carried a distinct karyotype (chromosome 9, 12, and 15 gain) and lacked the typical chromosome 22 loss that was used to define tumour cells in the original publication (Fig. 7C, SFig. 7E).

The LDA topics above were defined on developing meninges, but tumours are found in postnatal brains. As an alternative indicator of cell identity, we therefore next identified layer-specific genes expressed preferentially in adult meninges (exactly as previously described for Figure 4). Examining their expression in tumour cells, we found that in each subtype of tumour cells, the dura score dominated, while arachnoid was never among the top three. Only the pia score approached that of dura, and only in pericytes (Fig. 7D). These observations provide strong evidence in favour of a dural cell identity in meningiomas.

Gene expression can provide evidence for the cell of origin, but it remains possible that the fully developed tumour has taken on an identity different from the cell of origin. As an independent line of evidence based on cancer genomics, we reasoned that most cancer driver genes must be normally expressed in the cell of origin — or how else would they transform that cell? We therefore collected the 20 most frequently mutated genes in meningioma (COSMIC Cancer Browser, SFig. 7H) and analysed their collective expression in adult and fetal meninges. Intriguingly, the cell type with by far the highest expression of these putative meningioma cancer drivers in the developing meninges was the inner dura-dura, followed by committed dura precursors. (Fig. 7E-F, left). In healthy adult meninges, putative meningioma driver genes were expressed preferentially in inner dura cells (Fig. 7E-F, right). To reduce the influence of common cancer driver genes shared with other cancer types, we repeated the analysis after removing genes commonly mutated also in glioblastoma, intestinal cancer or in pancreatic cancer (Table S8). In each case, inner dura-dura and/or committed dura precursors remained the most enriched for expression of cancer drivers (SFig. 7G-L). These results lend further independent support to dural cells as the origin of meningioma, and particularly singles out inner dura cells as the most likely candidate. We therefore propose a model whereby meningioma tumours arise from cells of the dural lineage (Fig. 7G).

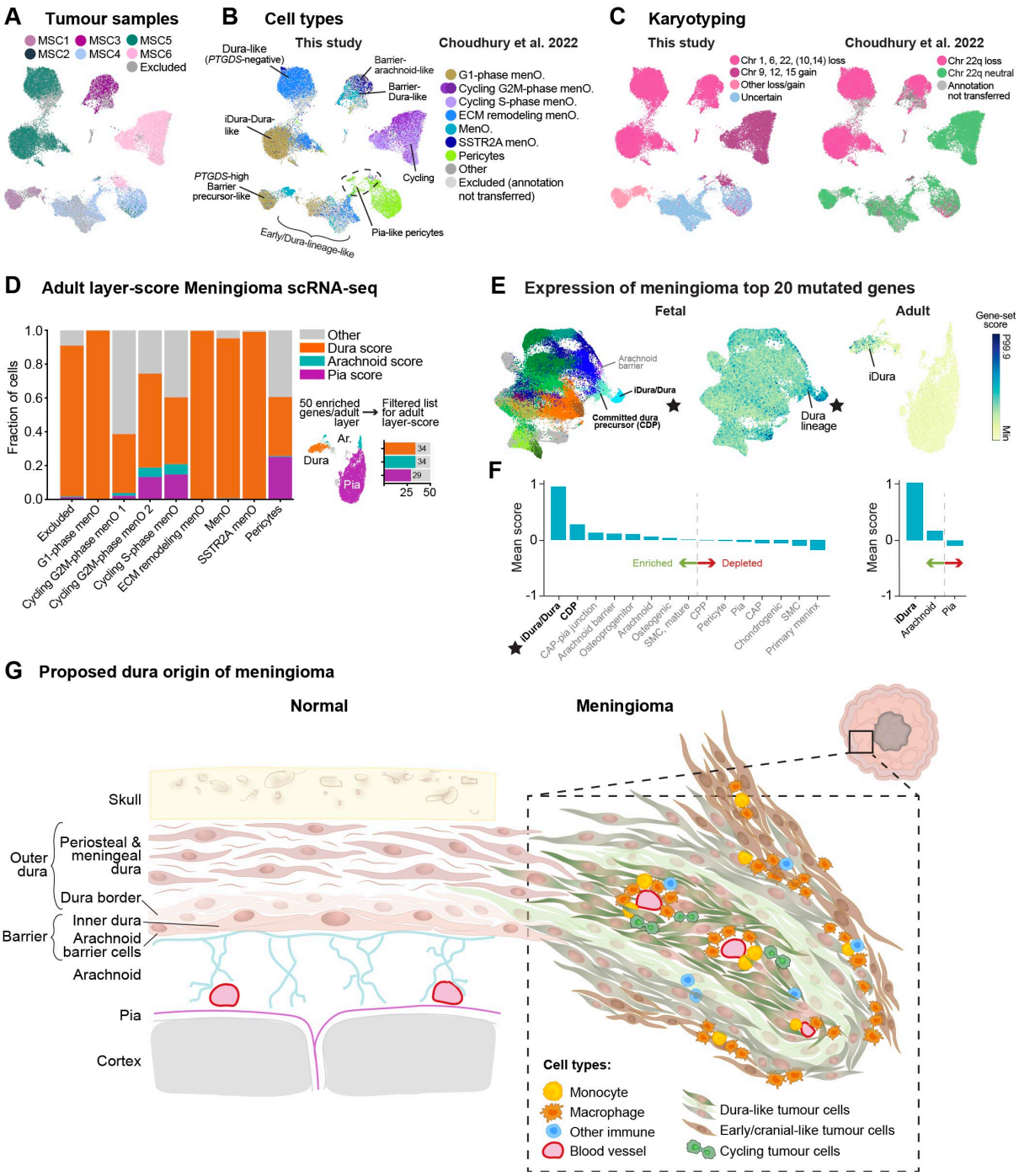

Figure 7. Genetic analysis supporting a dura origin of meningioma tumours

(A) UMAP of tumour cells and pericytes, coloured by samples. Data from Choudhury et al. (2022)[18].

(B) UMAP coloured by transferred annotations[18], with additional annotations added in this study. Arach., arachnoid; ECM, extracellular matrix; iDura, inner dura; MenO, meningioma.

(C) UMAP coloured by karyotype.

(D) Stacked bar chart showing the fraction of tumour cell types expressing enriched genes from adult meningeal layers (as in Figure 4). Lane for immune cells not shown in Figure, since we focused on tumour cells.

(E) Left: UMAP of fetal fibroblasts and perivascular cells, coloured by Subclass. Right: UMAPs of fetal fibroblasts and perivascular cells and adult fibroblasts[11], coloured by a gene-set score of the top 20 mutated genes in meningioma (https://cancer.sanger.ac.uk/cosmic/browse/tissue, Table S8).

(F) Mutated genes-score as in (E) quantified per fetal Subclass. Stars indicate the same cells across (E-F). CDP, committed dura precursor.

(G) Schematic illustration of healthy meninges, and the proposed formation of meningioma tumours from dura cells.

DISCUSSION

Fibroblasts and mesenchymal cells are poorly described in general, partly due to their unconventional lineage plasticity[43,44]. This often leads to ambiguous descriptions of cellular subtypes and function, and poor subtype markers (e.g. the canonical marker *COL1A1* is expressed in fibroblasts, all perivascular cells, and osteochondral cells). Spatial transcriptomics greatly aided a more detailed and accurate annotation of fetal craniofacial and meningeal fibroblasts. By using scRNA-seq and spatial transcriptomics we molecularly described the earliest progenitors of pia, arachnoid and dura mater. We also showed that meningeal layer development is defined by gene expression gradients, and occurs concurrently (Fig. 4).

Hypothesis of inner dura cells as a second barrier sheet on top of the arachnoid

Importantly, we discovered a fibroblast type transcriptionally similar to dura cells (*FXYD5*, *SLC47A1*) but expressing *CDH1*; i.e. 'inner dura' cells. In the fetal meninges, these cells formed a single sheet directly on top of *CDH1*+ arachnoid barrier precursor cells (Fig. 5). The current literature reports that only arachnoid barrier cells express *CDH1*[39], and a scRNA-seq atlas of the adult human leptomeninges annotated *CDH1*+*PTGDS*+ cells as the arachnoid barrier[10]. The first scRNA-seq paper of mouse E14.5 *Col1a1*+ cells found two clusters expressing *Cdh1*, one arachnoid (cluster 'M3') and one dura ('M4'). However, it was reported that only the 'M3' arachnoid cluster expressed tight junction genes[7]. Interestingly, our inner dura cells expressed many genes encoding a functional tight junction, and looked more like arachnoid barrier than outer dura cells histologically. This raises the intriguing possibility that the inner dura layer is epithelial (*CDH1*), and that the complete meningeal barrier is formed by two layers of cells; the inner dura and the arachnoid barrier. This model is further supported by electron microscopy[9], which has shown the meningeal barrier to be formed by precisely two layers of cells. It would also agree with the fact that in our tissue samples, the inner dura cells remained attached to the arachnoid (not the rest of the dura) at sites where the meninges had partially ruptured. Our findings are not necessarily inconsistent with mouse models of arachnoid barrier layer development[45], but show that the use of *CDH1* (and *PTGDS*) does not discriminate between the arachnoid barrier and inner dura, and therefore propose that the composition of the 'arachnoid barrier' may include the inner dura. If future experiments confirm this hypothesis, we propose renaming the arachnoid barrier to the 'arachnoid-dura barrier', and the *CDH1*+ inner dura cells to 'dura barrier cells'.

Hypothesis of meningioma cell of origin as dura cells, probably inner dura

Meningiomas have been described based on their location and histological subtypes, and classified based on atypical features like mitosis, and invasion[3]. However, they don't always behave according to their grade, in terms of unexpected recurrences and malignant transformations[46]. Recent efforts have refined meningioma classifications based on integrative multidimensional molecular profiling, and paired them with clinical parameters to more accurately reflect clinical outcomes[47–50]. Surprisingly though, meningiomas have not been described based on their molecular similarity to meningeal layers. Potentially, this has been due to the longstanding acceptance of the meningothelial arachnoid cell origin[51,52], and the existence of very few meningeal molecular and cellular atlases[7–10] to compare with. Here, we leveraged our comprehensive atlas of human meninges development to show that meningiomas contain cells similar to cells of the dura lineage. Instead, arachnoid topics were depleted (Fig. 6). Evidence supporting more specifically inner dura cells as a meningioma progenitor cell, was that they (1) expressed *CDH1*, as did meningioma, (2) were located in the meningeal barrier, consistent with previous anatomical evidence, (3) histologically looked like arachnoid barrier cells, (4) of all the topics, inner dura cells (topic 30) were the most consistent in all meningiomas (Fig. 6), and (5) expressed cancer driver genes. The fact that genetic driver genes of meningioma were enriched in inner dura cells (Fig. 7) suggests that these cells are particularly vulnerable to cancer transformation.

Previous studies were able to generate meningiomas from *PTGDS*-expressing primordial meningeal cells in mouse-models[4,53]. However, we demonstrated that *PTGDS* doesn't distinguish the arachnoid barrier from the inner dura. While our conclusion contradicts the current view of arachnoid meningothelial cells as the cell of origin for meningiomas, our findings are not necessarily inconsistent with previous findings, just that they did not discriminate between arachnoid barrier and inner dura cells experimentally and histologically. Furthermore, considering the clinical diversity of meningioma tumours it is likely that other progenitor cells drive or contribute to meningioma tumorigenesis as well, such as, for example, *NOTCH3*+ mural cells[5].

Limitations of the study

Fetal tissue availability was a limiting factor, for example, we miss PCW 11 meninges (Fig. 1). The majority of dura cells in our scRNA-seq atlas expressed *CDH1* (Fig. 5), therefore, we captured mostly inner dura. Likewise, we aspired to collect the arachnoid and whole dura from adult patients for spatial analysis, but due to surgical limitations we mostly obtained the dura border to some periosteal dura.

To confirm barrier function of the inner dura, the expression of tight junction proteins need to be confirmed, together with functional experimentation. Hence, we presented the results of our analysis as a hypothesis for the inner dura forming a barrier with the arachnoid barrier cells.

In this study, we mainly focused on hypermitotic grade 3 meningiomas for spatial transcriptomics (Fig. 6). However, meningiomas have 15 histological subtypes[54]. While we performed LDA topic transfer to bulk RNA-seq of 185 meningiomas (grades 1-3), further investigation is necessary to conclude whether our observations apply to other meningioma subtypes, or clinical parameters (age, sex, survival etc.).

RESOURCE AVAILABILITY

Lead contact

Further information and requests for resources and reagents should be directed to and will be fulfilled by the lead contact, Sten Linnarsson (sten.linnarsson@ki.se).

Materials availability

This study did not generate new unique reagents.

Data and code availability

- scRNA-seq: BAM files are available from the European Genome/Phenome Archive (https://ega-archive.org/) under accession number TBA. Count matrices are available from our companion GitHub page at https://github.com/linnarsson-lab/human-meninges-development.
- Xenium *in situ* data and images are available from the BioImage Archive under accession number S-BIAD1600 (https://www.ebi.ac.uk/bioimage-archive/).
- All original code for the analysis and visualisation of data has been deposited to our companion GitHub page at https://github.com/linnarsson-lab/human-meninges-development.
- All of the above are publicly available as of the date of publication.
- Any additional information required to reanalyse the data reported in this paper is available from the lead contact upon request.

ACKNOWLEDGMENTS

Firstly, we thank the donors for the samples used in this study. We thank Abrar Choudhury for transfer of meningioma metadata, and Kimberly Siletti for the initial implementation of LDA topic modeling. We thank Lars Borm for freezing and sharing the fetal heads. We thank Natalie Welsh, and Ezequiel Goldschmidt, for their insight about tight junctions and comparing the developing meninges and meningioma tumours respectively. We thank members of the Linnarsson lab for helpful discussions and lab management. We acknowledge Katarina Tiklova and the In Situ Sequencing Facility at SciLifeLab, funded by Science for Life Laboratory and the Swedish Research Council, for providing in situ sequencing services. We acknowledge support from the National Genomics Infrastructure in Stockholm, and the Biomedicum Imaging Core facility.

Funding: This study was supported by StratNeuro (E.V.); Erling-Persson Foundation Human Developmental Cell Atlas, Knut and Alice Wallenberg Foundation 2015.0041, 2018.0172 and 2018.0220, and EU Horizon2020 BRAINTIME project 874606, Swedish Research Council 2022-01248 (S.L.); NIH grants R01 CA262311 and P50 CA097257, and the Trenchard Family Charitable Fund (D.R.R.); The Royal Society (CDF/R1/241008) (S.W.). The Swedish Research Council (2024-02533) and Cancerfonden (24-3457) (M.N.).

AUTHOR CONTRIBUTIONS

Conceptualisation, E.V., and S.L.; scRNA sequencing, L.H., and E.V.; scRNA data preprocessing, P.L.; scRNA data analysis, E.V., P.L., and S.L.; B lineage analysis and visualisation, S.W.; immunohistochemistry, I.K., and E.V.; Xenium data processing, S.M.S.; Xenium data analysis, E.V., and S.M.S.; data annotation, E.V.; visualisation, E.V.; data curation and software, P.L., and S.M.S.; resources, X.H., R.A.B., E.S., X.L., D.R.R., M.N., M.H., and O.P.; writing - original draft, E.V., S.L., and S.W.; funding acquisition, S.L., M.N., and E.V.

All authors read and approved the final version of the manuscript.

DECLARATION OF INTERESTS

S.L. is a paid scientific advisor to Moleculent AB, and majority shareholder in EEL Transcriptomics AB (holding patents related to multiplex RNA detection in situ). S.M.S. is a co-founder of spatialist AB, a consulting company specialised in spatial omics analysis.

SUPPLEMENTAL INFORMATION

Document S1. Figures S1-S7
Table S1. Samples
Table S2. scRNA-seq cluster metadata
Table S3. Xenium probe panels
Table S4. Xenium clusters
Table S5. CSF analysis, related to Figure S3
Table S6. Network analysis, related to Figures 5 and S5
Table S7. Topics filtered genes, related to Figures 6, S6, and S7
Table S8. COSMIC mutated genes, related to Figure 7 and S7

869 **REFERENCES**

870 1. Aldinger, K.A., Lehmann, O.J., Hudgins, L., Chizhikov, V.V., Bassuk, A.G., Ades, L.C., Krantz,
871 I.D., Dobyns, W.B., and Millen, K.J. (2009). FOXC1 is required for normal cerebellar
872 development and is a major contributor to chromosome 6p25.3 Dandy-Walker malformation.
873 Nat. Genet. *41*, 1037–1042.

874 2. Brastianos, P.K., Galanis, E., Butowski, N., Chan, J.W., Dunn, I.F., Goldbrunner, R., Herold-
875 Mende, C., Ippen, F.M., Mawrin, C., McDermott, M.W., et al. (2019). Advances in
876 multidisciplinary therapy for meningiomas. Neuro. Oncol. *21*, i18–i31.

877 3. WHO Classification of Tumours Editorial Board (2021). Central Nervous System Tumours 5th
878 ed. D. N. Louis, ed. (International Agency for Research on Cancer).

879 4. Kalamarides, M., Stemmer-Rachamimov, A.O., Niwa-Kawakita, M., Chareyre, F., Taranchon, E.,
880 Han, Z.-Y., Martinelli, C., Lusis, E.A., Hegedus, B., Gutmann, D.H., et al. (2011). Identification of
881 a progenitor cell of origin capable of generating diverse meningioma histological subtypes.
882 Oncogene *30*, 2333–2344.

883 5. Choudhury, A., Cady, M.A., Lucas, C.-H.G., Najem, H., Phillips, J.J., Palikuqi, B., Zakimi, N.,
884 Joseph, T., Birrueta, J.O., Chen, W.C., et al. (2024). Perivascular NOTCH3+ stem cells drive
885 meningioma tumorigenesis and resistance to radiotherapy. Cancer Discov. *14*, 1823–1837.

886 6. Gold, M.P., Ong, W., Masteller, A.M., Ghasemi, D.R., Galindo, J.A., Park, N.R., Huynh, N.C.,
887 Donde, A., Pister, V., Saurez, R.A., et al. (2024). Developmental basis of SHH medulloblastoma
888 heterogeneity. Nat. Commun. *15*, 270.

889 7. DeSisto, J., O'Rourke, R., Jones, H.E., Pawlikowski, B., Malek, A.D., Bonney, S., Guimiot, F.,
890 Jones, K.L., and Siegenthaler, J.A. (2020). Single-cell transcriptomic analyses of the developing
891 meninges reveal meningeal fibroblast diversity and function. Dev. Cell *54*, 43-59.e4.

892 8. Wang, A.Z., Bowman-Kirigin, J.A., Desai, R., Kang, L.-I., Patel, P.R., Patel, B., Khan, S.M.,
893 Bender, D., Marlin, M.C., Liu, J., et al. (2022). Single-cell profiling of human dura and
894 meningioma reveals cellular meningeal landscape and insights into meningioma immune
895 response. Genome Med. *14*, 49.

896 9. Pietilä, R., Del Gaudio, F., He, L., Vázquez-Liébanas, E., Vanlandewijck, M., Muhl, L., Mocci, G.,
897 Bjørnholm, K.D., Lindblad, C., Fletcher-Sandersjöö, A., et al. (2023). Molecular anatomy of adult
898 mouse leptomeninges. Neuron *111*, 3745-3764.e7.

899 10. Kearns, N.A., Iatrou, A., Flood, D.J., De Tissera, S., Mullaney, Z.M., Xu, J., Gaiteri, C., Bennett,
900 D.A., and Wang, Y. (2023). Dissecting the human leptomeninges at single-cell resolution. Nat.
901 Commun. *14*, 7036.

902 11. Siletti, K., Hodge, R., Mossi Albiach, A., Lee, K.W., Ding, S.-L., Hu, L., Lönnerberg, P., Bakken,
903 T., Casper, T., Clark, M., et al. (2023). Transcriptomic diversity of cell types across the adult
904 human brain. Science *382*, eadd7046.

905 12. Braun, E., Danan-Gotthold, M., Borm, L.E., Lee, K.W., Vinsland, E., Lönnerberg, P., Hu, L., Li,
906 X., He, X., Andrusivová, Ž., et al. (2023). Comprehensive cell atlas of the first-trimester
907 developing human brain. Science *382*, eadf1226.

908 13. Farmer, D.T., Mlcochova, H., Zhou, Y., Koelling, N., Wang, G., Ashley, N., Bugacov, H., Chen,
909 H.-J., Parvez, R., Tseng, K.-C., et al. (2021). The developing mouse coronal suture at single-cell
910 resolution. Nat. Commun. *12*, 4797.

911 14. Li, B., Li, J., Fan, Y., Zhao, Z., Li, L., Okano, H., and Ouchi, T. (2023). Dissecting calvarial bones
912 and sutures at single-cell resolution. Biol. Rev. Camb. Philos. Soc. *98*, 1749–1767.

913 15. Sankowski, R., Süß, P., Benkendorff, A., Böttcher, C., Fernandez-Zapata, C., Chhatbar, C.,
914 Cahueau, J., Monaco, G., Gasull, A.D., Khavaran, A., et al. (2024). Multiomic spatial landscape
915 of innate immune cells at human central nervous system borders. Nat. Med. *30*, 186–198.

916 16. Mortus, J.R., Zhang, Y., and Hughes, D.P.M. (2014). Developmental pathways hijacked by
917 osteosarcoma. Adv. Exp. Med. Biol. *804*, 93–118.

918 17. Okano, A., Miyawaki, S., Hongo, H., Dofuku, S., Teranishi, Y., Mitsui, J., Tanaka, M., Shin, M.,
919 Nakatomi, H., and Saito, N. (2021). Associations of pathological diagnosis and genetic
920 abnormalities in meningiomas with the embryological origins of the meninges. Sci. Rep. *11*,
921 6987.

922 18. Choudhury, A., Magill, S.T., Eaton, C.D., Prager, B.C., Chen, W.C., Cady, M.A., Seo, K., Lucas,
923 C.-H.G., Casey-Clyde, T.J., Vasudevan, H.N., et al. (2022). Meningioma DNA methylation
924 groups identify biological drivers and therapeutic vulnerabilities. Nat. Genet. *54*, 649–659.

925 19. Heaton, H., Talman, A.M., Knights, A., Imaz, M., Gaffney, D.J., Durbin, R., Hemberg, M., and
926 Lawniczak, M.K.N. (2020). Souporcell: robust clustering of single-cell RNA-seq data by genotype
927 without reference genotypes. Nat. Methods *17*, 615–620.

928 20. O'Byrne, S., Elliott, N., Rice, S., Buck, G., Fordham, N., Garnett, C., Godfrey, L., Crump, N.T.,
929 Wright, G., Inglott, S., et al. (2019). Discovery of a CD10-negative B-progenitor in human fetal
930 life identifies unique ontogeny-related developmental programs. Blood *134*, 1059–1071.

931 21. Goh, I., Botting, R.A., Rose, A., Webb, S., Engelbert, J., Gitton, Y., Stephenson, E., Quiroga
932 Londoño, M., Mather, M., Mende, N., et al. (2023). Yolk sac cell atlas reveals multiorgan
933 functions during human early development. Science *381*, eadd7564.

934 22. Jardine, L., Webb, S., Goh, I., Quiroga Londoño, M., Reynolds, G., Mather, M., Olabi, B.,
935 Stephenson, E., Botting, R.A., Horsfall, D., et al. (2021). Blood and immune development in
936 human fetal bone marrow and Down syndrome. Nature *598*, 327–331.

937 23. Popescu, D.-M., Botting, R.A., Stephenson, E., Green, K., Webb, S., Jardine, L., Calderbank,
938 E.F., Polanski, K., Goh, I., Efremova, M., et al. (2019). Decoding human fetal liver
939 haematopoiesis. Nature *574*, 365–371.

940 24. Vanlandewijck, M., He, L., Mäe, M.A., Andrae, J., Ando, K., Del Gaudio, F., Nahar, K.,
941 Lebouvier, T., Laviña, B., Gouveia, L., et al. (2018). A molecular atlas of cell types and zonation
942 in the brain vasculature. Nature *554*, 475–480.

943 25. Kalucka, J., de Rooij, L.P.M.H., Goveia, J., Rohlenova, K., Dumas, S.J., Meta, E., Conchinha,
944 N.V., Taverna, F., Teuwen, L.-A., Veys, K., et al. (2020). Single-cell transcriptome atlas of
945 Murine endothelial cells. Cell *180*, 764-779.e20.

946 26. Cao, J., O'Day, D.R., Pliner, H.A., Kingsley, P.D., Deng, M., Daza, R.M., Zager, M.A., Aldinger,
947 K.A., Blecher-Gonen, R., Zhang, F., et al. (2020). A human cell atlas of fetal gene expression.
948 Science *370*, eaba7721.

949 27. Winkler, E.A., Kim, C.N., Ross, J.M., Garcia, J.H., Gil, E., Oh, I., Chen, L.Q., Wu, D., Catapano,
950 J.S., Raygor, K., et al. (2022). A single-cell atlas of the normal and malformed human brain
951 vasculature. Science *375*, eabi7377.

952 28. Hupe, M., Li, M.X., Kneitz, S., Davydova, D., Yokota, C., Kele, J., Hot, B., Stenman, J.M., and
953 Gessler, M. (2017). Gene expression profiles of brain endothelial cells during embryonic
954 development at bulk and single-cell levels. Sci. Signal. *10*.
955 https://doi.org/10.1126/scisignal.aag2476.

956 29. Jain, A., Ang, P.S., Matrongolo, M.J., and Tischfield, M.A. (2023). Understanding the
957 development, pathogenesis, and injury response of meningeal lymphatic networks through the
958 use of animal models. Cell. Mol. Life Sci. *80*, 332.

959 30. Wilting, J., Papoutsi, M., Christ, B., Nicolaides, K.H., von Kaisenberg, C.S., Borges, J., Stark,
960 G.B., Alitalo, K., Tomarev, S.I., Niemeyer, C., et al. (2002). The transcription factor Prox1 is a
961 marker for lymphatic endothelial cells in normal and diseased human tissues. FASEB J. *16*,
962 1271–1273.

963 31. Wigle, J.T., Harvey, N., Detmar, M., Lagutina, I., Grosveld, G., Gunn, M.D., Jackson, D.G., and
964 Oliver, G. (2002). An essential role for Prox1 in the induction of the lymphatic endothelial cell
965 phenotype. EMBO J. *21*, 1505–1513.

966 32. Jung, E., Gardner, D., Choi, D., Park, E., Jin Seong, Y., Yang, S., Castorena-Gonzalez, J.,
967 Louveau, A., Zhou, Z., Lee, G.K., et al. (2017). Development and characterization of A novel
968 Prox1-EGFP lymphatic and Schlemm's canal reporter rat. Sci. Rep. *7*.
969 https://doi.org/10.1038/s41598-017-06031-3.

970 33. Antila, S., Karaman, S., Nurmi, H., Airavaara, M., Voutilainen, M.H., Mathivet, T., Chilov, D., Li,
971 Z., Koppinen, T., Park, J.-H., et al. (2017). Development and plasticity of meningeal lymphatic
972 vessels. J. Exp. Med. *214*, 3645–3667.

973 34. Dani, N., Herbst, R.H., McCabe, C., Green, G.S., Kaiser, K., Head, J.P., Cui, J., Shipley, F.B.,
974 Jang, A., Dionne, D., et al. (2021). A cellular and spatial map of the choroid plexus across brain
975 ventricles and ages. Cell *184*, 3056-3074.e21.

976 35. Guldbrandsen, A., Vethe, H., Farag, Y., Oveland, E., Garberg, H., Berle, M., Myhr, K.-M.,
977 Opsahl, J.A., Barsnes, H., and Berven, F.S. (2014). In-depth characterization of the
978 cerebrospinal fluid (CSF) proteome displayed through the CSF proteome resource (CSF-PR).
979 Mol. Cell. Proteomics *13*, 3152–3163.

980 36. Dayon, L., Cominetti, O., Wojcik, J., Galindo, A.N., Oikonomidi, A., Henry, H., Migliavacca, E.,
981 Kussmann, M., Bowman, G.L., and Popp, J. (2019). Proteomes of paired human cerebrospinal
982 fluid and plasma: Relation to blood-brain barrier permeability in older adults. J. Proteome Res.
983 *18*, 1162–1174.

984 37. Mosby, L.S., Bowen, A.E., and Hadjivasiliou, Z. (2024). Morphogens in the evolution of size,
985 shape and patterning. Development *151*. https://doi.org/10.1242/dev.202412.

986 38. Zhu, X.-J., Liu, Y., Dai, Z.-M., Zhang, X., Yang, X., Li, Y., Qiu, M., Fu, J., Hsu, W., Chen, Y., et
987 al. (2014). BMP-FGF signaling axis mediates Wnt-induced epidermal stratification in developing
988 mammalian skin. PLoS Genet. *10*, e1004687.

989 39. Betsholtz, C., Engelhardt, B., Koh, G.Y., McDonald, D.M., Proulx, S.T., and Siegenthaler, J.
990 (2024). Advances and controversies in meningeal biology. Nat. Neurosci. *27*, 2056–2072.

991 40. Peyre, M., Salaud, C., Clermont-Taranchon, E., Niwa-Kawakita, M., Goutagny, S., Mawrin, C.,
992 Giovannini, M., and Kalamarides, M. (2015). PDGF activation in PGDS-positive arachnoid cells
993 induces meningioma formation in mice promoting tumor progression in combination with Nf2 and
994 Cdkn2ab loss. Oncotarget *6*, 32713–32722.

995 41. La Manno, G., Siletti, K., Furlan, A., Gyllborg, D., Vinsland, E., Mossi Albiach, A., Mattsson
996 Langseth, C., Khven, I., Lederer, A.R., Dratva, L.M., et al. (2021). Molecular architecture of the
997 developing mouse brain. Nature *596*, 92–96.

998 42. Blei, D.M., Ng, A.Y., and Jordan, M.I. (2003). Latent Dirichlet Allocation. J. Mach. Learn. Res. *3*,
999 993–1022.

1000 43. LeBleu, V.S., and Neilson, E.G. (2020). Origin and functional heterogeneity of fibroblasts.
1001 FASEB J. *34*, 3519–3536.

1002 44. Plikus, M.V., Wang, X., Sinha, S., Forte, E., Thompson, S.M., Herzog, E.L., Driskell, R.R.,
1003 Rosenthal, N., Biernaskie, J., and Horsley, V. (2021). Fibroblasts: Origins, definitions, and
1004 functions in health and disease. Cell *184*, 3852–3872.

1005 45. Derk, J., Como, C.N., Jones, H.E., Joyce, L.R., Kim, S., Spencer, B.L., Bonney, S., O'Rourke,
1006 R., Pawlikowski, B., Doran, K.S., et al. (2023). Formation and function of the meningeal
1007 arachnoid barrier around the developing mouse brain. Dev. Cell *58*, 635-644.e4.

1008 46. Goldbrunner, R., Minniti, G., Preusser, M., Jenkinson, M.D., Sallabanda, K., Houdart, E., von
1009 Deimling, A., Stavrinou, P., Lefranc, F., Lund-Johansen, M., et al. (2016). EANO guidelines for
1010 the diagnosis and treatment of meningiomas. Lancet Oncol. *17*, e383-91.

1011 47. Nassiri, F., Liu, J., Patil, V., Mamatjan, Y., Wang, J.Z., Hugh-White, R., Macklin, A.M., Khan, S.,
1012 Singh, O., Karimi, S., et al. (2021). A clinically applicable integrative molecular classification of
1013 meningiomas. Nature *597*, 119–125.

1014 48. Driver, J., Hoffman, S.E., Tavakol, S., Woodward, E., Maury, E.A., Bhave, V., Greenwald, N.F.,
1015 Nassiri, F., Aldape, K., Zadeh, G., et al. (2022). A molecularly integrated grade for meningioma.
1016 Neuro. Oncol. *24*, 796–808.

1017 49. Chen, W.C., Choudhury, A., Youngblood, M.W., Polley, M.-Y.C., Lucas, C.-H.G., Mirchia, K.,
1018 Maas, S.L.N., Suwala, A.K., Won, M., Bayley, J.C., et al. (2023). Targeted gene expression
1019 profiling predicts meningioma outcomes and radiotherapy responses. Nat. Med. *29*, 3067–3076.

1020 50. Lucas, C.-H.G., Mirchia, K., Seo, K., Najem, H., Chen, W.C., Zakimi, N., Foster, K., Eaton, C.D.,
1021 Cady, M.A., Choudhury, A., et al. (2024). Spatial genomic, biochemical and cellular mechanisms
1022 underlying meningioma heterogeneity and evolution. Nat. Genet. *56*, 1121–1133.

1023 51. Yamashima, T., Kida, S., and Yamamoto, S. (1988). Ultrastructural comparison of arachnoid villi
1024 and meningiomas in man. Mod. Pathol. *1*, 224–234.

1025 52. Tohma, Y., Yamashima, T., and Yamashita, J. (1992). Immunohistochemical localization of cell
1026 adhesion molecule epithelial cadherin in human arachnoid villi and meningiomas. Cancer Res.
1027 *52*, 1981–1987.

1028 53. Boetto, J., Peyre, M., and Kalamarides, M. (2021). Mouse models in meningioma research: A
1029 systematic review. Cancers (Basel) *13*, 3712.

1030 54. Louis, D.N., Perry, A., Wesseling, P., Brat, D.J., Cree, I.A., Figarella-Branger, D., Hawkins, C.,
1031 Ng, H.K., Pfister, S.M., Reifenberger, G., et al. (2021). The 2021 WHO classification of tumors of
1032 the Central Nervous System: A summary. Neuro. Oncol. *23*, 1231–1251.

1033 55. Dobin, A., Davis, C.A., Schlesinger, F., Drenkow, J., Zaleski, C., Jha, S., Batut, P., Chaisson, M.,
1034 and Gingeras, T.R. (2013). STAR: ultrafast universal RNA-seq aligner. Bioinformatics *29*, 15–21.

1035 56. Shannon, P., Markiel, A., Ozier, O., Baliga, N.S., Wang, J.T., Ramage, D., Amin, N.,
1036 Schwikowski, B., and Ideker, T. (2003). Cytoscape: a software environment for integrated
1037 models of biomolecular interaction networks. Genome Res. *13*, 2498–2504.

1038 57. Szklarczyk, D., Kirsch, R., Koutrouli, M., Nastou, K., Mehryary, F., Hachilif, R., Gable, A.L.,
1039 Fang, T., Doncheva, N.T., Pyysalo, S., et al. (2023). The STRING database in 2023: protein-
1040 protein association networks and functional enrichment analyses for any sequenced genome of
1041 interest. Nucleic Acids Res. *51*, D638–D646.

1042 58. Marco Salas, S., Czarnewski, P., Kuemmerle, L.B., Helgadottir, S., Matsson-Langseth, C.,
1043 Tismeyer, S., Avenel, C., Rehman, H., Tiklova, K., Andersson, A. et al. (2023). Optimizing
1044 Xenium In Situ data utility by quality assessment and best practice analysis workflows. bioRxiv.
1045 https://doi.org/10.1101/2023.02.13.528102.

1046 59. McGinnis, C.S., Murrow, L.M., and Gartner, Z.J. (2019). DoubletFinder: Doublet detection in
1047 single-cell RNA sequencing data using artificial nearest neighbors. Cell Syst. *8*, 329-337.e4.

60. Tirosh, I., Izar, B., Prakadan, S.M., Wadsworth, M.H., 2nd, Treacy, D., Trombetta, J.J., Rotem, A., Rodman, C., Lian, C., Murphy, G., et al. (2016). Dissecting the multicellular ecosystem of metastatic melanoma by single-cell RNA-seq. Science *352*, 189–196.

61. Neftel, C., Laffy, J., Filbin, M.G., Hara, T., Shore, M.E., Rahme, G.J., Richman, A.R., Silverbush, D., Shaw, M.L., Hebert, C.M., et al. (2019). An integrative model of cellular states, plasticity, and genetics for glioblastoma. Cell *178*, 835-849.e21.

1090 **METHODS**

1091 **KEY RESOURCES TABLE**

1092

REAGENT or RESOURCE	SOURCE	IDENTIFIER
Antibodies		
Recombinant Anti-Ki67 antibody [B56]	Abcam	Cat# ab279653, RRID: AB_2934265
Aquaporin 1/AQP1 Antibody (1/22)	Santa Cruz Biotechnology	Cat# sc-32737, RRID: AB_626693
Anti-Iba1 antibody [EPR16588]	Abcam	Cat# ab178846, RRID: AB_2636859
Anti-alpha smooth muscle Actin antibody [SP171]	Abcam	Cat# ab150301
Goat anti-Mouse IgG (H+L) Highly Cross-Adsorbed Secondary Antibody, Alexa Fluor™ Plus 555	Thermo Fisher Scientific	Cat# A32727, RRID: AB_2633276
Goat anti-Rabbit IgG (H+L) Highly Cross-Adsorbed Secondary Antibody, Alexa Fluor™ 647	Thermo Fisher Scientific	Cat# A-21245, RRID: AB_2535813
Goat anti-Mouse IgG2b Cross-Adsorbed Secondary Antibody, Alexa Fluor™ 555	Thermo Fisher Scientific	Cat# A-21147, RRID: AB_2535783
Biological samples		
Fetal meninges	Karolinska Hospital (Danderyd & Huddinge), Addenbrooke's Hospital Cambridge	N/A
Fetal heads	Addenbrooke's Hospital Cambridge	N/A
Human adult dura	Karolinska Hospital (Department of neurosurgery)	N/A
Human meningioma	University of California San Francisco	N/A
Chemicals, peptides, and recombinant proteins		
Sodium hydrosulfite	Sigma-Aldrich	Cat# 71699
10× PBS, pH 7.4, RNase-free	Thermo Fisher Scientific	Cat# AM9625
Hematoxylin and Eosin Stain Kit	Vector laboratories	Cat# H-3502
Xylenes	Sigma-Aldrich	Cat# 534056
Entellan™ new	Sigma-Aldrich	Cat# 1.07961
Pierce™ 16% Formaldehyde (w/v), Methanol-free	Thermo Fisher Scientific	Cat# 28908
Pierce™ 20X TBS Buffer	Thermo Fisher Scientific	Cat# 28358
Triton™ X-100	Sigma-Aldrich	Cat# T8787
Normal goat serum	Thermo Fisher Scientific	Cat# 31873
BSA (30%)	Sigma-Aldrich	Cat# A9576
Hoechst 33258 solution	Sigma-Aldrich	Cat# 94403
Lectin HPA From *Helix pomatia* (edible snail), Alexa Fluor™ 488 Conjugate	Thermo Fisher Scientific	Cat# L11271
ProLong™ Gold Antifade Mountant	Thermo Fisher Scientific	Cat# P36930

Hibernate™-E Medium	Thermo Fisher Scientific	Cat# A1247601
2-Methylbutane	Sigma-Aldrich	Cat# M32631
Isopropanol	Sigma-Aldrich	Cat# 34863
Nuclease-free dH2O	Thermo Fisher Scientific	Cat# 10977035
Papain Dissociation System	Worthington	Cat# LK003150
Critical commercial assays		
Chromium Single Cell 3' GEM, Library & Gel Bead Kit v3, 16 rxns	10x Genomics	Cat# PN-1000075
Chromium Single Cell B Chip Kit, 48 rxns	10x Genomics	Cat# PN-1000073
Chromium i7 Multiplex Kit, 96 rxns	10x Genomics	Cat# PN-120262
Xenium Slides & Sample Prep Reagents	10X Genomics	Cat# 1000460
Xenium Decoding Reagents	10X Genomics	Cat# 1000461
Xenium Decoding Consumables	10X Genomics	Cat# 1000487
Xenium Human Lung Gene Expression Panel	10X Genomics	Cat# 1000601
Deposited data		
scRNA-seq, human fetal meninges	This Manuscript	https://cellxgene.cziscience.com/collections/7d66d871-091f-4602-9f42-85f86d2853e0
Xenium in situ, human fetal heads	This Manuscript	https://www.ebi.ac.uk/bioimage-archive/ , #S-BIAD1600
Xenium in situ, human meningioma	This Manuscript	https://www.ebi.ac.uk/bioimage-archive/ , #S-BIAD1600
Xenium in situ, human dura	This Manuscript	https://www.ebi.ac.uk/bioimage-archive/ , #S-BIAD1600
Xenium & scRNA-seq loom files	This Manuscript	https://github.com/linnarsson-lab/human-meninges-development?tab=readme-ov-file
Human fetal endothelial cells	Braun et al.[12]	doi: 10.1126/science.adf1226
Human adult fibroblasts	Siletti et al.[11]	doi: 10.1126/science.add7046
Mouse embryonic fibroblasts	La Manno et al.[41]	doi: 10.1038/s41586-021-03775-x
Meningioma scRNA-seq, bulk RNA-seq	Choudhury et al.[18]	doi: 10.1038/s41588-022-01061-8
CSF proteomics human adult	Guldbrandsen et al.[35], Dayon et al.[36]	doi: 10.1074/mcp.M114.038554, doi: 10.1021/acs.jproteome.8b00809
Oligonucleotides		
Human custom probe panel	10X Genomics	Table S3
Human Lung Gene Expression Panel	10X Genomics	https://www.10xgenomics.com/products/xenium-panels
Software and algorithms		
Cytograph	Siletti et al.[11]	https://github.com/linnarsson-lab/adult-human-brain/tree/main/cytograph
Souporcell	Heaton et al.[19]	https://github.com/wheaton5/souporcell
Tomotopy v0.12.2	Blei et al.[42]	https://bab2min.github.io/tomotopy/v0.13.0/en/
STAR v2.7.10a	Dobin et al.[55]	https://github.com/alexdobin/STAR
CellRanger v6.1.2	10X Genomics	https://www.10xgenomics.com/support/software/cell-ranger/latest

Cytoscape v3.10.1	Shannon et al.[56]	https://cytoscape.org
STRING v2.2.0	Szklarczyk et al. [57]	https://www.string-db.org
Xenium data processing	Salas et al.[58], this manuscript	https://www.biorxiv.org/content/10.1101/2023.02.13.528102v1
Code for analysis and visualisation	This manuscript	https://github.com/linnarsson-lab/human-meninges-development
Other		
Superfrost Plus™ Adhesion Microscope Slides	Epredia	Cat# J1800ABDH
ImmEdge Hydrophobic Barrier PAP Pen	Vector laboratories	Cat# H-4000
Microscope Cover Glasses No. 1, 24 × 50mm	Nordic biolabs	Cat# 101222
30 µm cell strainer (CellTrics)	Sysmex	Cat# 04-0042-2316
Cancer genes	COSMIC	https://cancer.sanger.ac.uk/cosmic/browse/tissue
Xenium in situ platform	10X Genomics	N/A

EXPERIMENTAL MODEL AND STUDY PARTICIPANT DETAILS

Donors

Human prenatal samples were collected from elective medical abortions at the Department of Gynecology, Danderyd Hospital and Karolinska Huddinge Hospital, and Addenbrooke's Hospital in Cambridge, following oral and written informed consent by the patient. In Sweden, the use of abortion material was approved by the Swedish Ethical Review Authority and the National Board of Health and Welfare. In the UK, approval from the National Research Ethics Service Committee East of England – Cambridge Central was obtained (Local Research Ethics Committee, 96/085).

Patient samples

Human dura samples and one meningioma sample ("SL123") were collected from the Karolinska Hospital with informed consent from the patients and with ethical approval from the Swedish Ethical Review Authority (2020-03505). The use of samples was approved by the Swedish Ethical Review Authority (2020-02096).

Meningioma samples were collected from the University of California San Francisco (UCSF), complied with all relevant ethical regulations, and was approved by the UCSF Institutional Review Board (13–12587, 17–22324, 17–23196 and 18–24633). As part of routine clinical practice at UCSF, all patients who were included in this study signed a written waiver of informed consent to contribute deidentified data to research projects.

Details about all samples can be found in Table S1.

METHOD DETAILS

Tissue sample collection

Human fetal meninges

14 samples of human prenatal meninges were used in this study, at post-conception weeks (PCW) 5-13. Two samples of fetal heads were used, at PCW 6 and 9.5. The post-conception age of the embryos and fetuses was estimated by information from the clinical ultrasound, last menstrual period, true crown-rump-length, and age-dependent anatomical landmarks.

For samples collected at the Karolinska Hospital, the tissue was immediately transported to the laboratory following abortion, and dissected in ice-cold 0.9% NaCl solution under sterile conditions

1127 within 1-2 hours post abortion. For scRNA-seq, meninges were dissected and kept in ice-cold
1128 Hibernate-E medium until further processing. For spatial analysis fetal heads were covered by
1129 Tissue-Tek Optimal Cutting Temperature compound (OCT) in cryomolds, snap-frozen in a slurry of 2-
1130 methylbutane (Sigma-Aldrich) and dry ice, and stored at -80°C pending sectioning.
1131
1132 For samples collected in Cambridge, tissues were dissected in a class II hood on the day of
1133 collection and stored in Hibernate-E medium at 4°C. The tissue was shipped to Sweden at
1134 refrigerated temperature, and delivered two days after abortion. The procedure is covered under
1135 ethics REC: 96/085.
1136
1137 Human adult dura
1138 Four dura samples were collected from patients undergoing surgery for low grade gliomas and
1139 subependymoma (i.e. non-invasive, and meninges unaffected). During surgery, dura was placed in
1140 Hibernate-E medium on ice, and transported as such. Upon arrival, samples were washed in fresh
1141 Hibernate-E, then embedded in OCT, and snap-frozen in 2-methylbutane and dry ice slurry. Samples
1142 were stored at −80°C until further use.
1143
1144 Human meningioma
1145 Six meningioma tumour samples that were resected from 1991 to 2016 and snap frozen were
1146 identified from an institutional biorepository and clinical database at the University of California San
1147 Francisco (UCSF), with an emphasis on high-grade meningiomas.
1148 WHO grading was performed using contemporary criteria outlined in the WHO 2016 and 2021
1149 classification of tumours of the central nervous system. Samples were shipped to Sweden on dry ice,
1150 and stored at −80°C. Upon use, samples were embedded in OCT for cryosectioning. “SL123”
1151 meningioma was collected at the Karolinska Hospital as the dura samples above.
1152
1153 ***Cell dissociation***
1154 Dissected meninges were processed around 6 to 48 hours after tissue collection, depending on the
1155 source (Karolinska Hospital/Cambridge). Tissues were stored at 4°C in Hibernate-E medium during
1156 transport from Cambridge and until processing. Ice cold Earle’s Balanced Salt Solution (Worthington)
1157 was carbogenated (95% O2/ 5% CO2) and used throughout the whole procedure. Meninges were
1158 dissociated using the Worthington’s Papain Dissociation System (Worthington)
1159 (Protocols.io, https://dx.doi.org/10.17504/protocols.io.xmbfk2n). Tissues were enzymatically digested
1160 at 37 °C for 10-15 min, followed by trituration using fire polished glass Pasteur pipettes. Cell
1161 suspensions were filtered through a 30µm cell strainer (CellTrics, Sysmex) and centrifuged for 5 min
1162 at 200 g to obtain cell pellets. Supernatants were carefully removed, and cells resuspended in small
1163 volumes of EBSS (depending on cell density). Cell concentrations were estimated using a counting
1164 haemocytometer (Bürker/Neubauer chamber) and diluted with EBSS until the desired concentrations
1165 were reached. All suspensions were kept on ice until loading on the 10X Chromium chips.

1166 ***Single-cell RNA sequencing***
1167 Droplet-based single-cell RNA sequencing was performed using the 10x Genomics Chromium Single
1168 Cell Kit v3. Single-cell suspensions concentrated at 800-1200 cells/ml were mixed with master mix
1169 and nuclease free water according to the Chromium manual, targeting 5000-10000 cells per reaction.
1170 12 PCR cycles were used for cDNA synthesis, and the rest of the library preparation was performed
1171 according to the manufacturer’s instructions (10X Genomics, Illumina). All libraries were sequenced
1172 on an Illumina NovaSeq 6000 using S4 to a target sequencing depth of 100,000 reads/cell.
1173 Sequencing saturation was examined for each sample using preseq
1174 (https://github.com/smithlabcode/preseq).
1175
1176 ***Cryosectioning***
1177 Fresh-frozen tissue was embedded in OCT as above. The tissue was acclimatised in the cryostat
1178 chamber, and the specimen/chuck was set to -16°C and the knife −14°C (both for fetal heads, dura,
1179 and meningiomas). The samples were sectioned at 10µm and collected on Xenium slides following
1180 the manufacturer's recommendations, or captured on Superfrost Plus Adhesion Microscope Slides for
1181 other stainings as below.
1182
1183

1184 ***Xenium In Situ Gene Expression***
1185 Fresh-frozen 10µm tissue sections were placed on Xenium slides. The next steps were performed at
1186 the In Situ Sequencing Facility at SciLifeLab. The tissue was fixed and permeabilized according to the
1187 Xenium Fixation and Permeabilization Protocol (Demonstrated Protocol CG000581). A predesigned
1188 Human Lung panel (289 genes) and a custom gene panel (100 genes, Table S3) were applied to the
1189 tissue. Probes were hybridized to target RNA, followed by ligation and enzymatic amplification to
1190 generate multiple copies of each RNA target, as outlined in the Probe Hybridization, Ligation, and
1191 Amplification User Guide (User Guide CG000582). The prepared Xenium slides were subsequently
1192 loaded onto the Xenium Analyzer for imaging and analysis, following the Decoding and Imaging User
1193 Guide (User Guide CG000584). Instrument software version 1.4.3.1 and software analysis version
1194 1.4.0.7 were used throughout the process.
1195
1196 ***Post-Xenium hematoxylin and eosin staining***
1197 To remove autofluorescence quencher from the post-Xenium slides, tissues were incubated in
1198 1.74mg/ml sodium hydrosulfite dissolved in Mili-Q water for 10 min. The slides were then rinsed three
1199 times in Mili-Q water for 1 min, followed by a 2 min wash with distilled water (dH_2O). The slides were
1200 subsequently washed three times with 1× PBS and three times with dH_2O for 5 min. Hematoxylin
1201 solution (Hematoxylin and eosin stain kit) was applied to each section for 1 min and rinsed in two
1202 changes of dH_2O. Bluing agent (Hematoxylin and eosin stain kit) was applied to each section for 15
1203 seconds and the slide was rinsed twice with dH_2O. The slide was dipped in ethanol and excess >
1204 99.5% ethanol was blotted off. Eosin Y solution (Hematoxylin and eosin stain kit) was applied to each
1205 section for 30 seconds and rinsed in ethanol. The sections were subsequently dehydrated in three
1206 changes of > 99.5% ethanol for 2 min each and rinsed in xylenes, before mounting with Entellan™
1207 new. The slide was left to solidify for 24 hours in a ventilated hood.
1208
1209 ***Immunohistochemistry cryosections***
1210 Fresh-frozen tissue samples were cryosectioned into 10µm sections and captured on Superfrost Plus
1211 Adhesion Microscope Slides. A hydrophobic barrier was drawn around tissue sections using
1212 ImmEdge Hydrophobic Barrier PAP Pen. The sections were fixed with 4% formaldehyde in 1× PBS
1213 for 10 min. The slides were subsequently washed with 1× TBS for 5 min, then washed with three
1214 changes of 0.025% Triton X-100 in 1× TBS for 5 min each with gentle agitation. The sections were
1215 incubated with 200 µl of 10% normal goat serum and 1% bovine serum albumin (BSA) in 1× TBS
1216 blocking solution per section for 2 hours at room temperature. A mixture of desired primary antibodies
1217 was prepared with following dilutions: 1:1000 Recombinant Anti-Ki67 antibody [B56] and either 1:100
1218 Aquaporin 1/AQP1 Antibody (1/22), 1:1000 Anti-Iba1 antibody [EPR16588], or 1:200 Anti-alpha
1219 smooth muscle Actin antibody [SP171] with 1% BSA in 1× TBS. The sections were incubated with the
1220 primary antibody mixture in a humidifying chamber at 4°C overnight. The slides were washed with two
1221 changes of 0.025% Triton X-100 in 1× TBS for 5 min each with gentle agitation. A mixture of
1222 secondary antibodies was prepared with following dilutions: 1:500 Goat anti-Mouse IgG (H+L) Highly
1223 Cross-Adsorbed Secondary Antibody Alexa Fluor™ Plus 555 (for use with Ki67 primary antibody) and
1224 either 1:500 Goat anti-Rabbit IgG (H+L) Highly Cross-Adsorbed Secondary Antibody Alexa Fluor™
1225 647 (for use with IBA1 or ACTA2 primary antibodies) or 1:500 Goat anti-Mouse IgG2b Cross-
1226 Adsorbed Secondary Antibody, Alexa Fluor™ 555 (for use with AQP1 primary antibody) with 1% BSA
1227 in 1× TBS. The sections were incubated with the secondary antibody mixture for 1.5 hours at room
1228 temperature in a dark staining chamber. Subsequently, the slide was washed with three changes of
1229 1× TBS for 5 min each in a dark humidifying chamber. A stain mixture was prepared containing 2
1230 µg/ml Hoechst 33258 and 1:200 Lectin HPA From Helix pomatia (edible snail) Alexa Fluor™ 488
1231 Conjugate in 1× TBS. The sections were incubated with the stain mixture for 30 min at room
1232 temperature in a dark staining chamber. The slides were washed with 0.025% Triton X-100 in 1 ×
1233 TBS for 30 min and subsequently washed in three changes of 1× TBS for 5 min each at room
1234 temperature in a dark staining chamber. The slides were washed in 1 × TBS for 30 min in a dark
1235 staining chamber, before mounting with ProLong™ Gold Antifade Mountant and a coverslip. The
1236 slides were left to solidify overnight in a dark staining chamber.
1237
1238 ***Immunohistochemistry free-floating tissue***
1239 Fresh meninges pieces were placed into a 12-well plate and fixed with 4% formaldehyde in 1× PBS
1240 for 10-15 min with gentle agitation. Subsequent steps were conducted as above but in a 12-well plate,
1241 with antibodies diluted in a volume of 1 ml/well to cover the tissue, and washed with 2 ml. Following
1242 the final washes, the floating meninges were placed on Superfrost Plus Adhesion Microscope Slides,

and excess liquid was carefully removed. They were then mounted with ProLong™ Gold Antifade Mountant and a coverslip as above, and left to solidify overnight in a dark staining chamber

Histology image acquisition

Histology image acquisition was performed on a Zeiss Axio Scan.Z1 slide scanner with Zen Blue v3.1 acquisition software, using the Plan-Apochromat 20x/0.8 M27 objective with NA 0.8. For acquiring brightfield images (Hematoxylin and eosin staining) Hitachi HV-F203SCL camera (pixel size of 4.4 µm) with VIS-LED illumination source were used. For acquiring fluorescence images Hamamatsu ORCA-Flash4.0 V3 Digital CMOS camera (pixel size of 6.5 µm) with a Colibri 7 LED light source (100% intensity), PBS 405 + 493 + 575 + 654 + 761 beamsplitter, and PBP 425/30 + 514/31 + 592/25 + 681/45 + 785/38 emission filters. Namely, the following configurations were used: H3258 channel (Hoechst stain) was imaged using LED-Module 385 nm and BP 385/30 excitation filter; AF488 channel (Lectin HPA Alexa Fluor 488 conjugate) was imaged using LED-Module 475nm and BP 469/38 excitation filter; AF555 channel (Goat anti-Mouse IgG Highly Cross-Adsorbed Secondary Antibody, Alexa Fluor Plus 555, Goat anti-Mouse IgG2b Cross-Adsorbed Secondary Antibody, Alexa Fluor 555) was imaged using LED-Module 567 nm and BP 555/30 excitation filter; AF647 channel (Goat anti-Rabbit IgG Highly Cross-Adsorbed Secondary Antibody, Alexa Fluor 647) was imaged using LED-Module 630 nm and BP 631/33. Histology image acquisition was performed at Karolinska Institutet's Biomedicum Imaging Core facility (https://ki.se/en/bic).

Alignment of Xenium and histology images

H&E images are provided in the Xenium data folders (BioImage Archive, accession number S-BIAD1600). To align H&E files to the Xenium data, the correct .ome file, and .csv alignment file needs to be opened in the Xenium browser.

QUANTIFICATION AND STATISTICAL ANALYSIS

scRNA-seq data preprocessing

Illumina runs were demultiplexed with cellranger mkfastq version 6.1.2 (10x Genomics). Read mapping and unique molecular identifier (UMI) counts were determined using STARSolo[55] version 2.7.10a, using human genome GRCh38.p12 and transcript annotations from ENSEMBL release 93 from reference package GRCh38-3.0.0 as available from 10Xgenomics (www.10xgenomics.com). STARSolo was run with the following parameters:

```
--soloType CB_UMI_Simple
--soloCellFilter EmptyDrops_CR <expectedNcells> 0.99 10 45000 90000 500 0.01 20000 0.01 10000
--soloCBmatchWLtype 1MM_multi_Nbase_pseudocounts
--soloUMIfiltering MultiGeneUMI_CR
--soloUMIdedup 1MM_CR
--clipAdapterType CellRanger4
--outFilterScoreMin 30
```

Replicates were pooled, resulting in one loom file (loompy.org) per sample.

Quality control

Samples were analysed with "cytograph qc" (https://github.com/linnarsson-lab/adult-human-brain), which uses a modified version of DoubletFinder to calculate a doublet score for each cell[59]. We captured a median 13062 cells from each sample and then filtered cells based on their total number of mRNA molecules—as counted by unique molecular identifiers (UMIs)—and percentages of unspliced RNA, as well as doublet scores. Cytograph qc was initially run with standard parameters, where cells with fewer than 1000 UMIs, unspliced molecule fraction less than 0.1, or a doublet score below 0.4 were removed from further analysis. A second round of QC was performed after clustering (below). After QC, a final dataset containing 156,726 cells remained. Mean cells, genes and UMIs per sample are in Table S1. Variability across donors likely reflected the quality of the tissue.

Clustering

Cells were clustered using an updated version of the Cytograph package (https://github.com/linnarsson-lab/adult-human-brain). All cells that passed QC were pooled into a single dataset for initial clustering. The command "cytograph build" was run with configuration factorization: HPF, nn_space:

HPF, n_factors: 94, steps: nn, embeddings, clustering, aggregate, export. Default values were used for other parameters.

To get finer clusters, these top-level clusters were split by the dendrogram using the command "cytograph split --method dendrogram". Fibroblasts, neural, and vascular cells were split one more time by the dendrogram such that no split had more than 37 clusters. A second round of more stringent quality control was performed, whereby a cluster was removed if at least 40% of cells in the cluster had fewer than 1800 UMIs, or if we manually spotted clusters containing doublets or *HBB* (erythrocyte) contamination. Then, the splits were pooled into final subsets; Subset_Neural, Subset_Neural_crest, Subset_Epithelial, Subset_Fibroblasts, Subset_Perivascular, Subset_Endothelial, Subset_Immune, Subset_Erythropoietic (Table S2). Subset clusters were annotated and analysed separately, and also pooled into a final complete dataset containing all 245 clusters (Table S2; All_cells). UMAP embeddings were calculated for each subset, and the pooled dataset of all cells.

Annotation

Clusters were manually annotated as CellType based on literature, regional, and age composition (Table S2). Three additional levels of annotations were provided, on broader levels; "Subclass", "Class", and "Superclass". We computed cell cycle scores as previously described[41]. We used the expression of a set of well-known cell cycle genes[60] as a proxy for active proliferation. We calculated the cell cycle score as the fraction of UMIs those genes represented, and then the percentage of cells per cluster with a cell cycle score > 0.01. We also computed gene enrichment as previously described[41], and available in deposited Jupyter Notebooks (https://github.com/linnarsson-lab/human-meninges-development). Briefly, gene enrichment is a measure of overexpression in a cluster relative to other clusters, taking into account both mean expression and fraction of non-zero cells.

Maternal calling by SNP analysis

We used Souporcell as created by Heaton et al., 2020[19], and freely available at https://github.com/wheaton5/souporcell, applying it to the output from the STARSolo runs. Souporcell uses variants detected in scRNA-seq reads to assign cells to their donor of origin. In order to make sure that we applied Souporcell correctly, we first ran it on a dataset collecting separate maternal and fetal samples (data not shown) before analysing our own dataset.

Processing of Xenium's spatial datasets

Four types of samples were profiled using Xenium: (1) developmental human meninges (PCW 6), (2) developmental human meninges (PCW 9.5), (2) adult human dura and (3) meningioma samples. Due to the differences expected between each of the sample types, each of the sample types were processed independently using Scanpy (Code availability).

Processing of developmental and adult meningeal Xenium datasets

For developmental (PCW 6 and PCW 9.5) heads and adult dura samples, cells were first loaded and combined into a single AnnData object. With the aim of minimising the segmentation errors caused by Xenium's segmentation pipeline, only transcripts identified within segmented nuclei were kept for each of the profiled cells. This approach discards a considerable amount of the profiled reads but minimises potential mis-segmentation effects (Marco Salas et al., 2023[58]). Only transcripts annotated as genes in the provided panel were retained. Cells were then filtered to remove low-quality observations, discarding cells with less than eight detected genes or fewer than 20 total transcripts. After this, expression values were normalised to a total count of 10,000 transcripts per cell, followed by logarithmic transformation. Highly variable genes were identified based on specific thresholds of mean expression and dispersion, and principal component analysis (PCA) was performed to reduce dimensionality. The neighbourhood graph was constructed using the top 50 principal components, and clustering was conducted using the Leiden algorithm. A UMAP 2D representation was generated to visualise cell clusters, and the processed data were saved. Based on the spatial location and differentially expressed genes identified for every cluster, clusters were annotated assigning a cell type to each high-quality cell profiled. For developmental datasets (PCW 6 and PCW 9.5), due to the complexity of both mesenchymal and neural clusters, these clusters were independently subclustered in a subsequent analysis (Code availability), integrating the resulting annotations into a final object containing a cell type assigned to each high-quality cell profiled.

Processing of meningioma Xenium datasets

Due to the high biological variability between tumour samples, meningioma's processing was done on a tumour-basis, combining only replicates of the same tumour when available. In here, quality control measures were also applied to filter out cells with fewer than three detected genes or fewer than five total transcripts. Expression data were normalised to a total count of 10,000 transcripts per cell, followed by a logarithmic transformation. Principal component analysis (PCA) was used to reduce dimensionality, with the top 50 principal components selected to capture major sources of variation in the dataset. A neighbourhood graph was constructed using the top 40 components, enabling (1) the application of the Leiden algorithm to identify clusters and (2) a low-dimensional representation of the data, using UMAP.

B lineage analysis

We produced dotplots to visualise gene expression, using raw gene expression count matrices subset to cell types of interest as input. We then normalised these count matrices using the Scanpy (v1.9.3) sc.pp.normalise_per_cell function with counts_per_cell_after=1e4. A ln(x+1) transformation was then applied to the normalised counts using the sc.pp.log1p function. Gene expression was then visualised using the sc.pl.dotplot function. To increase interpretability of plots, the vmax argument was sometimes used to apply an upper limit to the color scale (where used, noted within GitHub scripts). Data produced in this study was compared to data from fetal bone marrow as B-cell reference (Jardine et al., 2021)[22], and yolk sac (Goh et al., 2023)[21].

Neftel score

We independently reimplemented the gene profile scoring algorithm from Neftel et al., 2019[61], and generalised it to work with any given set of genes. Our implementation in Python is provided as neftel_score.py, and we confirmed that our code reproduces the original analysis from Neftel et al.

Fibroblast layer-maturation score

Fibroblasts from the snRNA-seq data from Siletti et al., 2023[11] was downloaded, and top 50 enriched genes per meningeal layer calculated. Three criteria were imposed to filter the gene lists such that they contained genes that are highly expressed, and after PCW 6.

1. Criteria to be considered expressed in PCW 5-6: >15% of cells should have at least one transcript of the gene. If expressed in PCW 5-6, these genes were removed so that the gene list reflects genes involved in maturation of the meningeal layers.
2. Criteria to be considered expressed: Gene count above 2.
3. Criteria to be considered pia/arachnoid/dura: At least 5% of the enriched genes should be expressed in a cell to not become "Other".

STRING Network and pathways analysis

The gene expression values of a list of bioactive molecules, and enriched genes, for the inner dura and arachnoid barrier clusters was analysed and visualised using Cytoscape version 3.10.1 (Shannon et al., 2003[56]). The expression of bioactive molecules and enriched genes were analysed (1) as uniquely expressed by the inner dura or arachnoid barrier, and (2) as shared between the two. STRING database[57] version 2.2.0 was used to visualise networks of interconnected molecules (50% confidence for node connectivity), belonging to significantly enriched pathway ontologies (Table S6). Pathway analysis in STRING is based on KEGG, Reactome, and Wiki Pathways.

Topic modeling with Latent Dirichlet Allocation (LDA)

LDA[42] was used to identify transcriptional modules that vary across cells, and also reveals co-expressed genes in single-cell data. We used tomotopy version 0.12.2 to perform topic modeling with LDA. Model training, identification of topic-representative genes, and other general parameters were performed as previously described[11]. Here, the number of topics "k" generated were 35. Some topics were specific to quality, for example *HBB* erythrocyte contamination, mitochondrial or ribosomal genes, and one topic contained genes from the Y-chromosome. Some topics were not specific or did not seem to be biologically meaningful. Therefore, we manually chose topics of interest. We also identified representative genes for each topic by using the topic probabilities reported for each gene (function "get_topic_word_dist"). We filtered genes by specificity (topic probabilities for each gene normalized by that gene's probability across all topics) and then sorted the remaining genes by their unnormalized probabilities (Table S7). A script is available as optimize_lda.py

at github.com/linnarsson-lab/adult-human-brain, and scripts of its application in this study are available at https://github.com/linnarsson-lab/human-meninges-development.

LDA also allows you to score new cells for a given gene topic. Hence, we validated the scRNA-seq topic annotations by transfer to spatial data (scoring spatial data for the LDA topics generated on scRNA-seq data).

Transfer of scRNA-seq LDA topics to Xenium in situ gene expression data

Topics from the model were transferred to matching genes in the Xenium dataset and the weights obtained used to colorize the *in situ* images.

Transfer of scRNA-seq LDA topics to bulk RNA-seq data

Bulk RNA-seq data of 185 meningiomas was downloaded from Choudhury et al. (2022)[18] and split according to their methylation group; Merlin-intact, Immune-enriched, and Hypermitotic. For each tumor and tumor type, the relative contribution of each topic was calculated, and sums were normalized to 1.0.

Reanalysis of meningioma scRNA-seq data

Downloaded from Choudhury et al. (2022)[18] and processed with the same Cytograph pipeline as described for the fetal meninges scRNA-seq data generated in this study. Tumour cells (fibroblast-like) and pericytes were isolated into a new loom file, to keep the comparison consistent with the fetal meningeal fibroblasts and pericytes.

Computational expression-based karyotyping

We inferred chromosomal copy number aberrations by determining normalized gene expression along chromosomes, using a normal brain atlas (Siletti et al. 2023)[11] as the reference. By using an external reference, we avoided the need to manually identify normal cells within each sample. We normalized expression in each cell to the median total UMIs across all cells. We included only genes from the autosomes that were expressed at more than 10% of the 99th percentile expression level in at least half of the clusters in the reference atlas. Then, for each cell in the sample, we identified the reference cell type (cluster in the atlas) with the greatest correlation coefficient. For each cell, we then computed a ploidy score along the chromosomes by dividing the normalized expression in the cell by the normalized expression in the reference cell type and multiplying by two. We smoothed the ploidy along the chromosomes in windows of 25 genes and then normalized the resulting ploidy to the median ploidy and multiplied by two. We used the resulting ploidy vectors (one for each cell in the sample) as the input for a clustering procedure: we computed the first five principal components, calculated a nearest-neighbour graph (k=30 neighbours) and used Leiden graph clustering to find metacells having similar ploidy profiles. Finally, for each metacell we used a hidden Markov model to infer integer chromosomal copy numbers. The detailed Python code implementing this algorithm is provided as hmm_karyotyper.py, which also provides visualization of the result.

Expression of COSMIC mutated genes in fetal meningeal fibroblasts

The Catalogue of Somatic Mutations in Cancer (COSMIC) Cancer Browser (https://cancer.sanger.ac.uk/cosmic/browse/tissue) version 98-99 was used to find the top 20 mutated genes in meningioma, glioblastoma (Astrocytoma Grade IV), intestinal carcinoma, and prostate adenocarcinoma. Overlapping genes between cancers were removed, to ensure that generic cancer drivers didn't have an effect (Table S8).